UNIVERSITY OF OKLAHOMA

GRADUATE COLLEGE

EXPERIMENTAL STUDIES OF CESIUM RYDBERG ATOM PAIR INTERACTIONS

A DISSERTATION

SUBMITTED TO THE GRADUATE FACULTY

in partial fulfillment of the requirements for the

Degree of

DOCTOR OF PHILOSOPHY

By

KIM RICHARD OVERSTREET II
Norman, Oklahoma
2009

EXPERIMENTAL STUDIES OF CESIUM RYDBERG ATOM PAIR INTERACTIONS

A DISSERTATION APPROVED FOR THE
HOMER L. DODGE DEPARTMENT OF PHYSICS AND ASTRONOMY

BY

Dr. James P. Shaffer, Chair

Dr. Gregory Parker

Dr. Michael Morrison

Dr. Eric Abraham

Dr. Michael Santos

Dr. Zhisheng Shi

This thesis is dedicated to my wife Miho and dog Nico.

Acknowledgements

I would first like to thank Arne Schwettmann. The calculations and simulations that he performed were critical to understanding the experimental results and were significant on their own. I would also like to thank Jonathan Tallant for help with the measurements and the AutoCAD work that went into fig. 3.10. Patrick Zabawa also deserves credit for his work on the Mathematica program to calculate the inverse Abel transforms of CCD images of the MOT. Also, I would like to thank Donald Booth for his help analyzing the potentials for the macrodimer measurements. Lastly I would like to thank my advisor Professor James P. Shaffer, who gives new meaning to the phrase, "light a fire under your ass". I think mine is well done. This work could not have been finished without everyone's help.

Contents

List of Figures

List of Tables

Abstract

This thesis describes experimental studies of Rydberg atom pair interactions. A new technique is described that combines trapping of ultracold Cesium atoms with Rydberg tagging time-of-flight spectroscopy to attain a velocity resolution of 2.5 cm/s. Using this technique, observed molecular resonances in Cesium spectra are characterized as either dissociating photo-initiated collision processes or bound long range Rydberg atom-Rydberg atom molecules called macrodimers.

Chapter 1

Introduction

The purpose of this work was to experimentally observe a new class of long range Rydberg atom-Rydberg atom molecules that occur due to avoided crossings between Rydberg atom pair potentials in an electric field. This class of molecules can remain bound at long range ($\sim \mu$m) or dissociate as a fast collision process. The nature of the pair process will depend strongly on the magnitude of the applied field due to the extreme sensitivity of Rydberg atoms to electric fields. These experiments have been motivated by work with resonant energy transfer in Rydberg gases [1], predictions of long range bound molecular states [2], proposals for using Rydberg atoms for quantum information using dipole blockade [3, 4], and experimental observations of pair resonances in ultracold Rydberg gases [5, 6].

The primary driving force behind studies of Rydberg pair interactions is the phenomenon known as dipole blockade. Dipole blockade was proposed as a method for generating entangled states in Rydberg gases [3, 4]. The dipole-dipole interaction is strong enough, that the excitation of a single Rydberg atom creates a local field that can block the excitation of a second Rydberg atom (see fig. 1.1). The second atom sees an energy shift Δ due to the field created by the excited atom that drives the transition frequency out of resonance with the laser field. The effect of dipole blockade on optical excitation lineshapes has been observed in several experiments [7–9]. The strength of the dipole-dipole interaction and the long coherence times

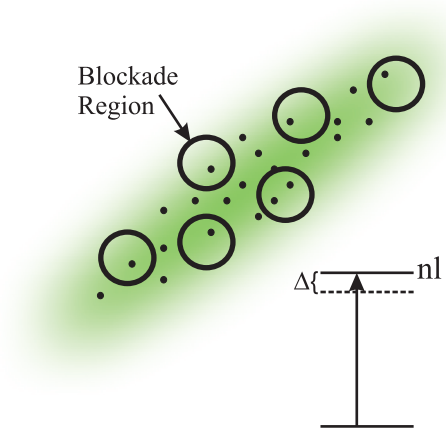

Figure 1.1: Diagram of a gas of atoms with circles indicating the blockade region due to an excited Rydberg atom. The energy required to excite another atom within the blockade radius is shifted by Δ.

make Rydberg states ideal for quantum computation schemes [3, 4]. The magnitude of Δ depends critically on the R dependence of the pair interaction potential.

Resonant energy transfer by collisions between atoms or molecules has been studied extensively due to applications in laser science and recently as applied to Rydberg atoms [1]. In Rydberg atoms, the effects can be much more dramatic because of the sensitivity of Rydberg atoms to electric fields.

Resonant energy transfer occurs when two atoms or molecules collide and exchange energy. In order for energy to be resonantly exchanged, both partners must have an accessible transition that is equal in energy. This does not occur often in nature and the existence of such an energy match is rare. In Rydberg states however, the energy spacings can be easily modified so that such a coincidence can be realized using the Stark effect (see fig. 1.2). By applying an electric field, the energy levels can be shifted to enhance the probability of resonant transfer of energy. As an example, consider the collision,

$$nS + nS \rightarrow (n-1)P + nP. \tag{1.1}$$

This collision would not be resonant at zero field because the transition $nS \rightarrow nP$

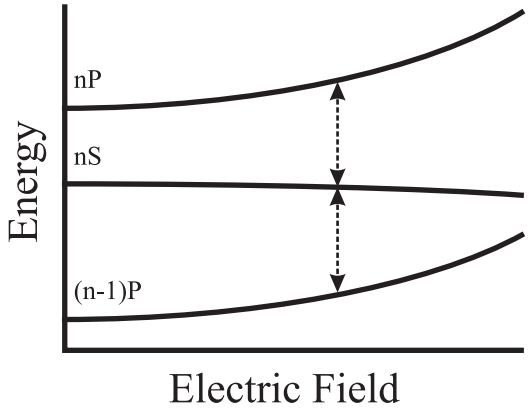

Figure 1.2: Energy level diagram of an atom in the presence of an electric field. The dashed line indicates the electric field where the transition of an nS state upward to nP equals that downward to $(n-1)P$.

does not equal $nS \rightarrow (n-1)P$ in energy. By applying an electric field, the nS state will have a negative Stark shift while the P states will experience a positive shift. At some electric field, the upward and downward transition from the nS state will be equal, allowing for resonant transfer of energy.

The long range nature of the interaction between pairs of Rydberg atoms can have strong effects on the shape of spectral profiles [10]. The idea of exciting Rydberg atom pairs that interact by a long range potential is similar to photoassociation, with the enhanced tunability of the energy states with an applied electric field and the larger length scale ($\sim \mu m$). Fioretti et al. observed resonant energy transfer in ultracold Cs that could be explained by the interaction of pairs of Rydberg atoms at long range. The observed spectral profiles displayed asymmetry that was explained in the context of long range pair interactions [10]. Their observations suggested that the attractive or repulsive nature of the interaction determined the asymmetry of the spectral profiles.

The dipole-dipole interaction alone is not sufficient to fully describe the interaction between two Rydberg atoms. In order to understand the pair interactions, detailed calculations of the higher order multipole interactions (dipole-dipole, dipole-quadrupole and quadrupole-quadrupole) are required [11, 12]. Perturbative calcu-

lations alone do not account for the resonant, near resonant and off resonant interactions. To accurately describe the interactions, matrix diagonalization is necessary [12]. Together with accurate calculations, it is possible to explain experimental observations of interacting pairs of Rydberg atoms.

It has been proposed that the multipolar interactions between pairs of Rydberg atoms could lead to bound molecular states [2]. Macrodimers are exotic states that consist of two Rydberg atoms that are bound at extremely long range ($R > 1\,\mu$m). Predicting bound states that may be formed by avoided crossings requires accurate calculations of the pair interaction potentials in the presence of small electric fields. While the initial prediction of these long range molecular states was predicted using perturbative calculations [2], calculations using matrix diagonalization with an applied field showed that the existence of macrodimers was likely [13]. The calculations in [2] ignored the interactions between the pair states that give rise to avoided crossings. The work described in this thesis depends critically on the existence of avoided crossings for the formation of bound states.

Further experiments were soon underway to investigate the physics of the long range interactions [5–8]. An experiment was conducted by Oliveira et al. which measured the time evolution of the atomic population due to energy transfer for the Rubidium collision process [5],

$$33P_{3/2} + 33P_{3/2} \rightarrow 33S_{1/2} + 34S_{1/2}. \tag{1.2}$$

Their experimental observations were in qualitative agreement with predictions based on a semiclassical model of two Rydberg atoms colliding under the influence of a R^{-5} potential, including effects from radiative decay. Quantitative agreement was not achieved due to insufficient knowledge of the pair interaction potential.

An important experiment was performed by Farooqi et al. in which the first direct excitation of pair resonances was observed [6]. In ion yield spectra in Rubid-

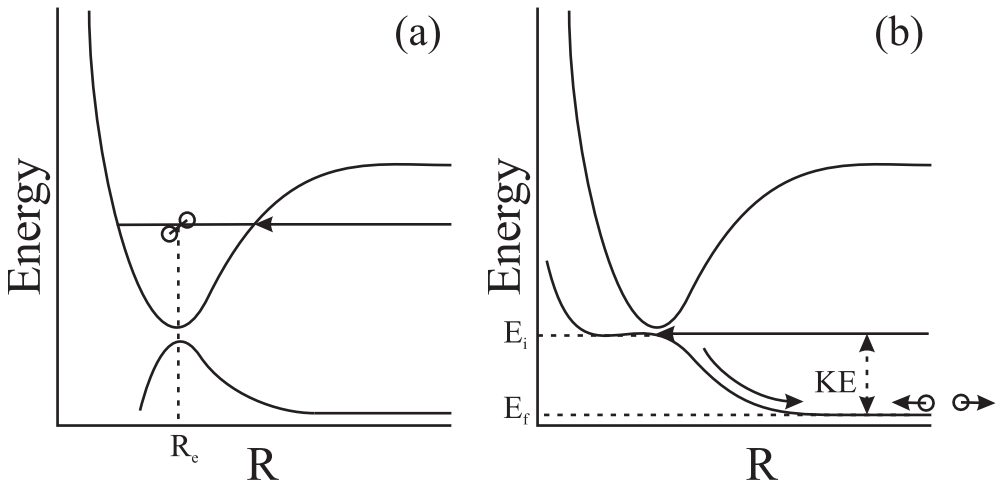

Figure 1.3: Avoided crossings that lead to the formation of (a) bound states and (b) photo-initiated collisions. The range of R is $\sim 10\,\mu$m in both figures. An excited macrodimer will remain bound in the well, while a collision will result in atomic fragments that recoil with a kinetic energy KE determined by the energy of the exit channel, E_f.

ium, resonance features were observed that did not correspond to atomic Rydberg states. These molecular resonances were observed at energies that corresponded to pair excitations of Rydberg atoms. The resonances were verified to be due to pairs of Rydberg atom by measurements of the excitation rate dependence on the optical excitation intensity, but did not necessarily correspond to bound molecular states. The avoided crossings in the long range potentials that give rise to bound molecular states can also give rise to photo-initiated collisions (see fig. 1.3) [14]. Fig. 1.3 (a) shows a diagram of a well that could result from an avoided crossing. Excitation of a vibrational state or states of the well would result in a molecule that oscillates about its equilibrium position R_e. Collision processes can occur by excitation at a stationary point in the pair interaction potentials, with internal energy that is then converted to translational motion along R as shown in fig. 1.3 (b). The pair will be excited with energy E_i and gain kinetic energy KE that is equal to

$$KE = E_i - E_f \tag{1.3}$$

as determined by the energy E_f of the exit channel. It is not possible to determine if an excited pair remains bound or dissociates with purely spectroscopic methods. A pair could be bound at the time of creation and then dissociate by coupling to a repulsive pair state. The probability of predissociation will depend on the energy spacing of the pair interaction potentials and the coupling between the states.

The primary focus of this thesis work was to observe the signatures of photo-initiated collision processes and the existence of macrodimer molecules. The measurements were conducted by observing the dynamics of the fragments as they either receded by dissociation or remained bound. Such a signature was measured by monitoring the expansion of the fragments as a function of time after excitation of the molecular complex. These methods lay the foundations for future studies that wish to produce these exotic molecules for sensitive tests of theory [2]. The high fidelity achieved also paves the way for future studies of ultracold collisions between atoms and diatoms and further experimental studies of ultracold chemistry. By extending the time-of-flight methods described in this work to full 3-dimensional measurements of product spatial distributions, it would be possible to study the potential energy surface that determines many-body collision dynamics.

Chapter 2

Physics of Rydberg States

In this chapter I will discuss the relevant characteristics of Rydberg states. The energy level structure of Rydberg states will be discussed, including the relevant parameters for Cs (quantum defects, etc.). I will discuss the lifetime of high n Rydberg states, modified by the effects of blackbody radiation. I will also summarize the basic theory of the long-range pair interactions that can give rise to avoided crossings that could support bound or dissociative states.

2.1 Energy of Rydberg States

The energy levels for the Rydberg states of Cs are obtained by replacing the principal quantum number n for Hydrogen with an effective principal quantum number $n^* = n - \delta_{nl}$ where δ_{nl} is the quantum defect. The energy spectrum is

$$E_{nl} = -\frac{R_{Cs}}{(n^*)^2} \tag{2.1}$$

where $R_{Cs} = 3.289828299(20) \times 10^9\,\mathrm{MHz}$ is the Cs Rydberg constant [15] and the zero of energy is at ionization (a sample spectrum can be seen in fig. 2.1). At high $n\,(\sim 100)$, the energy spacing between Rydberg states is ∼GHz. The quantum defect arises from a phase shift that occurs in the electronic wavefunction of the valence electron due to the ionic core. The core electrons shield the valence electron from the

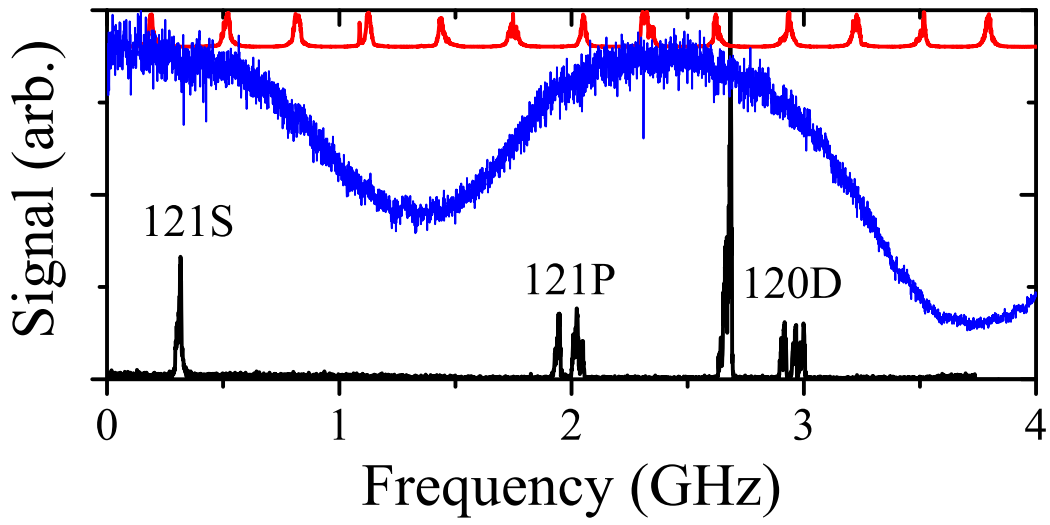

Figure 2.1: A spectrum of high n Rydberg states of Cs (in black). A simultaneous Fabry-Perot signal with a free spectral range of 300 MHz is shown in red. A simultaneous reference spectrum of molecular Iodine is shown in blue. The zero of frequency for this spectrum was arbitrarily chosen.

nuclear core which causes a phase shift equal to δ_{nl}/π (see fig. 2.2) [16].

As is indicated from the notation, the quantum defect is also slightly n dependent. The quantum defect is given by the expansion,

$$\delta_{nl} = \delta_0 + \frac{\delta_2}{(n-\delta_0)^2} + \frac{\delta_4}{(n-\delta_0)^4} + ... \tag{2.2}$$

where the parameters are taken from [15, 16] and are tabulated in table 2.1.

Series	δ_0	δ_2
$nS_{1/2}$	4.049325(15)	0.246(5)
$nP_{1/2}$	3.591556(30)	0.3714(40)
$nP_{3/2}$	3.559058(30)	0.374(40)
$nD_{3/2}$	2.475365(20)	0.5554(60)
$nD_{5/2}$	2.466210(15)	0.0167(5)
$nF_{5/2}$	0.033392(50)	-0.191(30)
$nF_{7/2}$	0.033537(28)	-0.191(20)

Table 2.1: Quantum defect parameters for Cs. The quantum defects for $l > 3$ are effectively zero as are the parameters $\delta_{\geq 4}$ [15, 16].

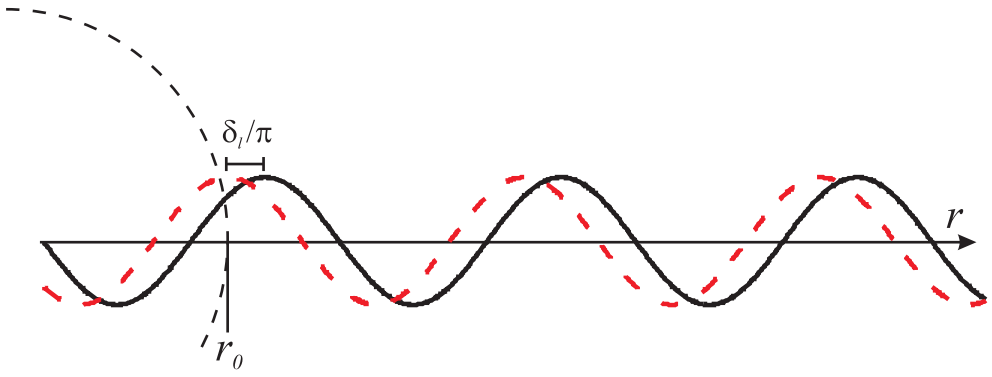

Figure 2.2: Diagram of the radial wave functions for hydrogen (solid black) and an alkali (red dashed). The ionic core of an alkali pulls the phase of the wavefunction towards the ionic core with radius r_0 by an amount δ_{nl}/π.

2.2 Model Potential of the Core

In order to solve for the wavefunctions of Cs, it is necessary to model the interaction of the valence electron with the core. For a review of model potential methods, the reader is referred to [17]. The model must describe the motion of the valence electron in the presence of the core electrons in a way that reproduces the energy structure of the atom of interest, in this case Cs.

The potential that was used in this work was that given by Marinescu et al. [18]. The potential was obtained by a five-parameter parametric fit to the Rydberg energies of Cs. The model potential is

$$V_l(r) = \frac{Z_l(r)}{r} - \frac{\alpha_c}{2r^4}\left[1 - e^{-(r/r_c)^6}\right] \tag{2.3}$$

where

$$Z_l(r) = 1 + (z-1)e^{-a_1 r} - r(a_3 + a_4 r)e^{-a_2 r}. \tag{2.4}$$

Parameter	$l = 0$	$l = 1$	$l = 2$	$l \geq 3$
a_1	3.49546309	4.69366096	4.32466196	3.01048361
a_2	1.47533800	1.71398344	1.61365288	1.40000001
a_3	-9.72143084	-2465624280	-6.70128850	-3.20036138
a_4	0.02629242	-0.09543125	-0.74095193	0.00034538
r_c	1.92046930	2.13383095	0.93007296	1.99969677

Table 2.2: Model potential parameters for Cs from [18].

z is the nuclear charge and r_c truncates the nonphysical effects of the core at short r. $\alpha_c = 15.644$ is the core polarization of Cs. The parameters for the model potential of Cs is given in table 2.2.

2.3 Lifetimes of Rydberg States

The length of time that a pair of Rydberg atoms can interact will be limited by their individual lifetimes. The lifetime of a Rydberg state can be anywhere from $\sim \mu$s up to several ms. However, blackbody radiation can have a strong influence on the effective lifetime of a Rydberg state [16]. The spectrum of the blackbody radiation can cause stimulated emission into nearby Rydberg levels due to the high density of states.

The effective transition rate (Γ_{eff}) of a Rydberg state will be the sum of the natural radiative decay rate (Γ_{rad}) and the blackbody decay rate (Γ_{bb}) or in terms of the lifetimes

$$\frac{1}{\tau_{eff}} = \frac{1}{\tau_{rad}} + \frac{1}{\tau_{bb}}. \tag{2.5}$$

The effective lifetime τ_{eff} can be predicted from theoretical calculation of τ_{rad} and τ_{bb}. He et al [19] expressed the natural radiative decay as a polynomial sum

$$\tau_{rad} = a_0 + a_1(n^*) + a_2(n^*)^2 + a_3(n^*)^3 \tag{2.6}$$

where a_i are l dependent parameters (see table 2.3). Farley and Wing derived an

Series	a_0	a_1	a_2	a_3
nS	2.47	1.72	-0.247	1.2
nP	-102	21.5	0.831	2.53
nD	4.51	4.20	0.0553	0.661

Table 2.3: a_i parameters for calculation of the radiative lifetime of Cs. The a_i parameters have units of ns [19].

approximate expression for τ_{bb} for $n^* \gtrsim 12.8$ [20],

$$\frac{1}{\tau_{bb}} = \frac{4}{3}\left(\frac{e^2}{\hbar c}\right)^3 \left(\frac{kT}{\hbar}\right) \frac{1}{n^{*2}}. \tag{2.7}$$

2.4 Stark Effect

It is important to account for the Stark effect in Rydberg gases as most experiments are conducted with the application of an electric field. Even the most carefully constructed apparatus can have a small stray electric field that must be considered for an accurate description of the system. The Stark effect is given by an extra term in the Hamiltonian

$$H_s = \boldsymbol{d} \cdot \boldsymbol{E} \tag{2.8}$$

where we will only consider the valence electron with induced dipole moment $\boldsymbol{d}$ to experience a static electric field $\boldsymbol{E}$. In order to find the energies of an alkali in an electric field, perturbation theory is not feasible due to the strong interaction between neighboring Rydberg states [21]. In Hydrogen, symmetry of the core allows identical m to cross, but in alkali atoms, this symmetry is broken by the core. Matrix diagonalization becomes the preferred method of calculating the energies.

The Stark effect for Hydrogen has a well known solution in parabolic coordinates [22]. The parabolic representation is no longer advantageous for alkalis because the Stark Hamiltonian is not diagonal in a parabolic basis due to the inclusion of fine structure. Computationally, it is then easier to use the spherical basis for diagonal-

ization [21].

The Stark interaction including fine structure with total angular momentum $j = l \pm 1/2$ for dipole transitions between states $|l', j', m_j'\rangle$ with energy W' and $|l, j, m_j\rangle$ with energy W has matrix elements

$$\langle W, l, j, m_j|zE_z|W', l', j', m_j'\rangle = \delta(m_j, m_j')\delta(l, l' \pm 1)\langle W, l|r|W', l'\rangle E_z$$
$$\times \sum_{m_l = m_j \pm 1/2} \langle l, 1/2, m_l, m_j - m_l|j, m_j\rangle\langle l', 1/2, m_l, m_j - m_l|j, m_j\rangle\langle l, m_l|\cos\theta|l', m_l\rangle. \tag{2.9}$$

The last term in eqn. 2.9 is evaluated

$$\begin{aligned}\langle l, m|\cos\theta|l-1, m\rangle &= \left(\frac{l^2 - m^2}{(2l+1)(2l-1)}\right)^{1/2}, \\ \langle l, m|\cos\theta|l+1, m\rangle &= \left(\frac{(l+1)^2 - m^2}{(2l+3)(2l+1)}\right)^{1/2}.\end{aligned} \tag{2.10}$$

Eqn. 2.9 can be diagonalized to obtain the Stark energies and Stark eigenfunctions. These eigenfunctions can then be used for calculating the pair interactions in the presence of an electric field.

2.5 Pair Interactions

The object of the experiments described in this thesis is to study the multipolar interactions between Cs Rydberg atom pairs. The theoretical framework for calculating the pair interactions was developed by Flannery, Vrinceanu, and Ostrovsky [11]. Calculations based on matrix diagonalization are necessary for a complete description of the interactions [11, 12]. It is also important to include electric field effects, as the effects can be strong even for small fields.

The multipole expansion for the interaction between two atoms A and B with

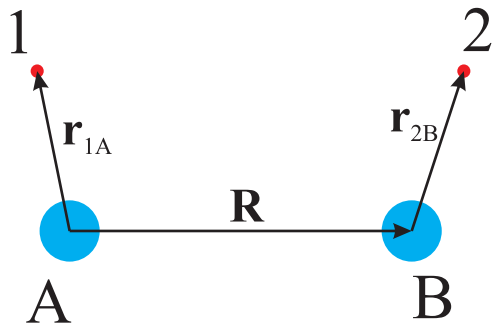

Figure 2.3: Two center coordinate system with nuclei A and B with electrons 1 and 2 respectively.

internuclear separation $\boldsymbol{R} = R\hat{z}$ is [11]

$$V(\boldsymbol{R}, \boldsymbol{r}_{1A}, \boldsymbol{r}_{2B}) = \sum_{L_1,L_2=1}^{N} \sum_{M=-L}^{L} \frac{(-1)^{L_2} f_{L_1 L_2 M}}{R^{L_1+L_2+1}} Q_{L_1 M}(\boldsymbol{r}_{1A}) Q_{L_2 -M}(\boldsymbol{r}_{2B}) \tag{2.11}$$

where the multipole operator with electronic coordinate $\boldsymbol{r}$ is

$$Q_{LM}(\boldsymbol{r}) = \{\frac{4\pi}{2L+1}\}^{1/2} r^L Y_{LM}(\hat{r}) \tag{2.12}$$

and

$$f_{L_1 L_2 M} = \frac{(L_1+L_2)!}{[(L_1+M)!(L_1-M)!(L_2+M)!(L_2-M)!]^2} \tag{2.13}$$

and Y_{LM} is the familiar spherical harmonic. Setting $N = 2$ limits the interactions to dipole-dipole, dipole-quadrupole, and quadrupole-quadrupole. By diagonalizing the Hamiltonian with the interaction of eqn. 2.11 in the Stark shifted atomic basis, potential energy curves of Cs Rydberg atom pairs (the pair potentials), have been calculated to high precision [12, 13]. The use of eqn. 2.11 is limited to R greater than the LeRoy radius, where effects such as exchange must be included [11]. The electric field in these calculations was aligned along the internuclear axis R. This choice greatly simplifies the calculation of the interaction. Anisotropic effects should be small for the length scales studied in this experiment considering the weak electric fields that are used ($\sim$mV/cm) [12, 13].

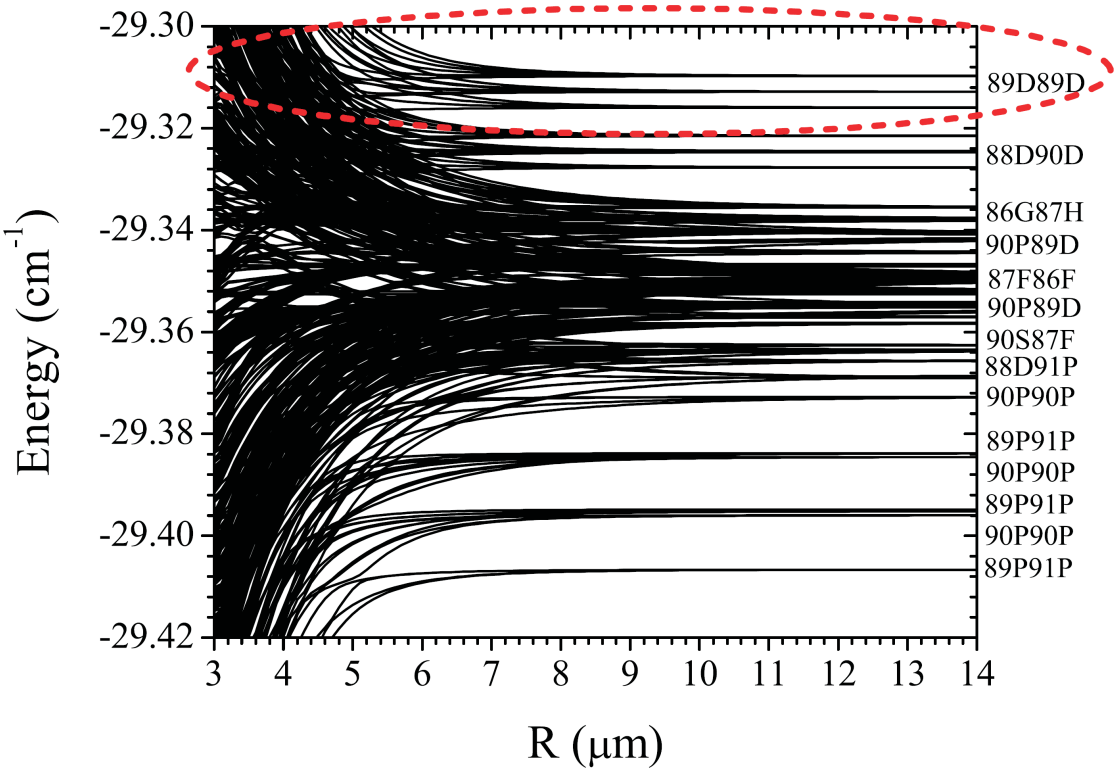

Figure 2.4: Calculated pair potentials in the vicinity of the 89D state of Cs (circled in red). The calculations shown here are for zero applied electric field.

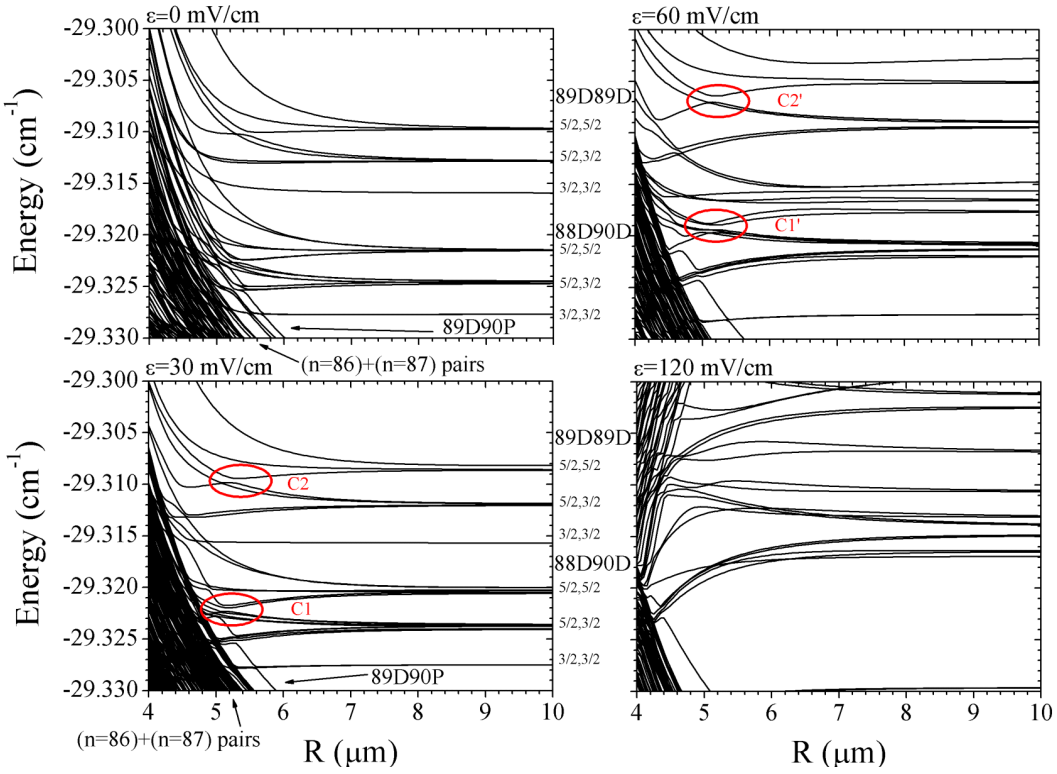

Figure 2.5: Pair potentials near the $89D + 89D$ pair energy with an applied electric field ε along R. The avoided crossings C1 and C2 give rise to wells that may support hundreds of bound states [13].

The pair potentials near the $89D$ state of Cs can be seen in fig. 2.4 and are taken from [12]. At high n, it is apparent that there are strong interactions between the states at short R that could give rise to avoided crossings. It is the purpose of this work to experimentally investigate the dynamics of the atom pairs in the vicinity of avoided crossings.

With the application of an electric field, the pair interactions can be modified. Fig. 2.5 shows the pair interaction potentials near the $89D + 89D$ pair for different electric fields ε. Avoided crossings at C1 and C2 can be enhanced with a small increase in applied field along R. These wells have been calculated to support hundreds of bound states with energy spacings on the order of kHz [13]. The density of the rovibrational states due to the width of the wells prevents spectroscopic observation of the bound state structure. The thermal broadening of the atomic sample would

blur the rovibrational structure even at ultracold temperatures.

Observation of the rovibrational structure would still not be sufficient to demonstrate that the molecules formed would remain bound. The energy spacing at the avoided crossing can lead to coupling to the lower dissociative state and prevent the stable formation of macrodimers. At lower n, the spacing becomes larger which would decrease the coupling to a nearby, lower energy repulsive state. The experimental search for stable macrodimer molecules would therefore be favorable at lower principal quantum number.

The pair potentials depend on n in two technically significant ways. As n is decreased, the pair interactions have a stronger effect at shorter R. This requires higher atomic densities to excite and will result in lower experimental yield. Also, the avoided crossings move further to the red of the nearby identical pair states. The nearby identical pair state is responsible for the enhanced excitation probability for pair excitation at the avoided crossings [13]. As n is decreased, the avoided crossings will move further from the nearby identical pair state and suffer a decrease in excitation probability resulting in lower experimental yield.

Chapter 3

Experimental Setup

The apparatus for these experiments was designed to measure small particle velocities. It consists of a magneto-optic trap (MOT) surrounded by a high resolution photo-fragment spectrometer. The spectrometer is designed so that the atomic fragments start from a highly localized region in space and are allowed to expand from the initial volume for a variable delay as neutrals. The excited fragments are then ionized and mapped onto the detector to observe the 1D mapping of their spatial distribution. In this section, I will first describe the basics of the MOT and then the custom diode laser systems that are used to cool the Cs atoms in the MOT. Second, I will describe the vacuum system and spectrometer. Last, I will describe density dependent effects that have been measured as a function of the trapping parameters.

3.1 The Cs Magneto-Optic Trap

The Cs samples for these experiments are prepared in a MOT. The relevant energy level structure can be seen in fig. 3.1. In short, atoms are cooled in a MOT by emitting a higher energy photon for each photon absorbed and confined spatially with the application of a inhomogeneous magnetic field. The advantage of the MOT is the high density of atoms at ultracold temperatures. The temperature and density of atoms within the MOT depend on the trapping laser intensity and detuning. The density will also depend on the magnetic field gradient. In this section I will describe

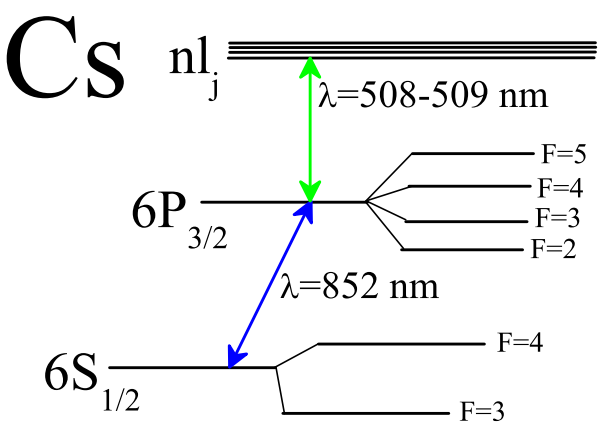

Figure 3.1: Relevant optical transitions in Cs for this work.

the cooling mechanisms in the MOT and how confinement is achieved.

The fundamental cooling mechanism that underlies the formation of ultracold atom samples is Doppler cooling. Doppler cooling occurs from the repeated absorption of photons from a specified direction, and re-emission into a random direction (see fig. 3.2). For cooling by laser light, the angular frequency of the cooling laser, ω_L, is seen Doppler shifted by the absorbing atom

$$\omega_L = \omega_0 - \mathbf{k} \cdot \mathbf{v} \tag{3.1}$$

where ω_0 is the frequency of the cooling transition, $\mathbf{k}$ is the wavevector of the laser light, and $\mathbf{v}$ is the velocity of the absorbing atom. The detuning of the laser beam is $\delta = \omega_L - \omega_0$. Dissipation of energy occurs due the emission of a higher energy photon than the energy of the absorbed photon. The atom will absorb the photon in the lab frame where the frequency is detuned, but will emit on resonance in its own rest frame, which dissipates an amount of energy $\hbar\delta$. Repeated absorptions and emissions will cool the atoms to the temperature determined by the natural linewidth of the cooling transition, to the so-called Doppler limit.

Doppler cooling damps the motion of atoms, but does not provide spatial confinement. The addition of a spatially varying restoring force is necessary to contain the

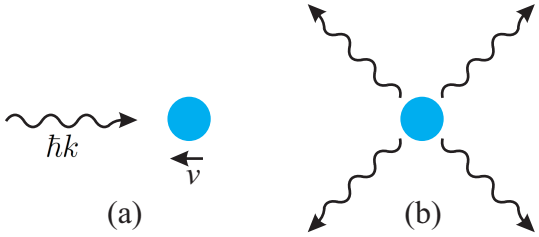

Figure 3.2: A photon is incident on an atom from a specified direction (a) and is radiated by spontaneous emission into a random direction (b).

cooled atoms in a localized region. If the atoms are Doppler cooled in the presence of an inhomogeneous but linearly varying magnetic field and by choosing the appropriate polarizations of the cooling light, the effective detuning, $\delta(z)$ will have a spatial dependence,

$$\delta_{\pm}(z) = \delta \mp \mathbf{k} \cdot \mathbf{v} \pm \frac{\boldsymbol{\mu} \cdot \mathbf{B}}{\hbar} \tag{3.2}$$

where μ is the transition magnetic moment and $B(z)$ is the magnetic field (see fig. 3.3).

By circularly polarizing two counter-propagating, red detuned cooling beams, selection rules dictate which magnetic sublevel of the excited state will absorb laser light from a specified direction. As the atom moves in the magnetic field, its magnetic sublevels will become shifted by a spatially varying amount. As the atoms move away from the center $B = 0$ region, the force on the atoms toward the center will be greater as they come into resonance with the appropriately polarized laser beam. Selection rules on Δm transitions are such that a $\Delta m = +1$ transition will occur for absorption of circular right (σ_+) polarized light and $\Delta m = -1$ transitions will occur for circular left (σ_-) polarized light. If the polarizations are set to correspond to the directional dependence of the Zeeman shift, the atoms will feel a confining force towards the center of the trap.

With this description of the cooling properties of the MOT, the temperature of the atoms would be limited to the Doppler temperature set by the natural linewidth of the atomic transition (125 μK for Cs), but polarization gradients within the MOT allow

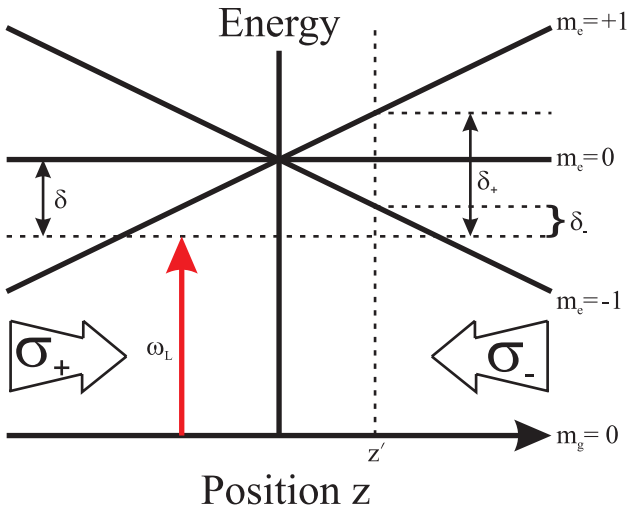

Figure 3.3: A diagram of the Zeeman splitting of the magnetic sublevels in an inhomogeneous magnetic field. σ_+ light drives $\Delta m = +1$ transitions when an atom moves to the left, and σ_- light drives $\Delta m = -1$ transitions when an atom moves to the right. The farther an atom moves away from the origin, the closer to resonance the cooling beams become. This induces a position dependent detuning $\delta_\pm$.

for cooling below this limit. The local polarization at the position of an atom shifts the internal energy allowing for what has been called polarization gradient cooling [23]. Local polarization gradients allow more energy to be dissipated from the system as the local light shift of the atoms' internal energy states are modified by the laser field. The light shift arises from the Stark effect of the electric field induced on the magnetic substates on the atom. The energy shift of the ground magnetic sublevels, the "light shift", is

$$\Delta E_g = \frac{\hbar\delta(I/I_s){C_{ge}}^2}{1+4(\delta\tau)^2} \tag{3.3}$$

where I is the intensity of the laser field, I_s is the saturation intensity of the transition, τ the lifetime of the excited state, and C_{ge} is the Clebsch-Gordan coefficient for the coupling of the atom to the light field [24]. The polarization affects the light shift through C_{ge} and provides additional energy dissipation as the atomic population is pumped between magnetic sublevels that have opposite signs for the light shift. This provides a highly efficient method for cooling atoms below the Doppler limit over many optical pumping cycles. This is the essence of polarization gradient cooling.

The temperature of the atoms within the MOT depend on the trapping laser detuning and intensity. The temperature for the MOT can be approximated as linear for temperatures less than the Doppler temperature, T_D. The temperature is approximated

$$T = T_0 + 2 \times C_\sigma T_D \left(\frac{\Omega^2}{|\delta|\Gamma} \right) \tag{3.4}$$

where $\Omega = \Gamma\sqrt{I/2I_s}$ is the Rabi frequency for a single laser beam, and Γ is the natural linewidth of the transition with saturation intensity I_s. For the Cs $6S_{1/2} \rightarrow 6P_{3/2}$ transition, $\Gamma = 5.22\,\mathrm{MHz}$ and $I_s = 1.1\,\mathrm{mW/cm^2}$ for $\sigma_\pm$ light. The term in parentheses is called the light shift parameter. T_0 is the low temperature limit for an operating MOT without cooling by alternative means (such as evaporative cooling). C_σ is the experimentally observed constant of proportionality for cooling with $\sigma_\pm$ polarized light.

The number of atoms in the MOT can be measured by observing the fluorescence emitted by the trapped atoms and can be combined with measurements of the trap size to find the density of the atoms in the MOT [25]. The density will determine the distribution of atomic pairs in the MOT that are at the internuclear separation relevant for a given interaction. Measurements of the fluorescence monitor the photon scattering rate which depends on δ and I. As the trapping laser is detuned or the trapping laser intensity decreased, the emitted fluorescence of the atomic sample will decrease. The scattering rate, R is approximated

$$R \simeq \hbar\omega_L \frac{\Gamma}{2} \frac{{C_1}^2\Omega^2/2}{\delta^2 + \Gamma^2/4 + {C_2}^2\Omega^2/2} \tag{3.5}$$

where ${C_1}^2 = {C_2}^2 = .73$ are the averaged Clebsch-Gordon coefficients taken from [25]. As more atoms become trapped, the density increases until the MOT becomes optically thick. This means a re-emitted photon has a higher probability of being reabsorbed before leaving the trap [33]. This effect is called "multiple scattering"

and it limits the maximum achievable density inside the MOT. As more atoms are cooled, the density cannot increase due to internal pressure from the rescattered photons, causing the volume of the MOT to increase. As a consequence, the spatial distribution of the MOT becomes non-Gaussian due to the uniform density region in its center. The rescattered light also acts to heat the gas, as it is resonant with the atomic transition, and is directed out of the trap.

3.2 Diode lasers

Two custom diode laser systems were constructed for cooling Cs. Diode laser systems are ideal in modern atomic physics experiments for their low cost, narrow linewidth, and low intensity noise. Typical linewidths for stabilized diode lasers are < 1 MHz and linewidths as low as a few hundred kHz can be achieved. With extreme effort, diode lasers can even be pushed to ∼Hz stability. Because the stability of the current supply limits the intensity stability, the intensity noise is typically $< 1\,\%$. Diode lasers' application to telecommunication has spurred their development, greatly benefiting research into ultracold atomic physics, and spectroscopy as a whole.

The two diode lasers used in these experiments are high power quantum well index guided laser diodes with powers of 180 mW (JDS Uniphase SDL-5401-G1) for the cooling laser and 70 mW (SDL-5421-G1) for the repumping laser. The diodes are mounted in commercial diode mounts (ThorLabs TCLDM9). The diode temperatures and currents are controlled using commercial controllers (ThorLabs TEC2000 and LDC500 respectively, see fig. 3.4).

The diode lasers are constructed using an extended cavity arrangement. The setup of a single laser system is shown in fig. 3.4. A diffraction grating (1200 lines/inch) is aligned so that the 0^{th} order is injected back into the diode for feedback. 25 % of the diode laser power is injected back into the diode in this way. The positioning of the grating can be coarse adjusted using fine-pitch screws attached to the mount. After

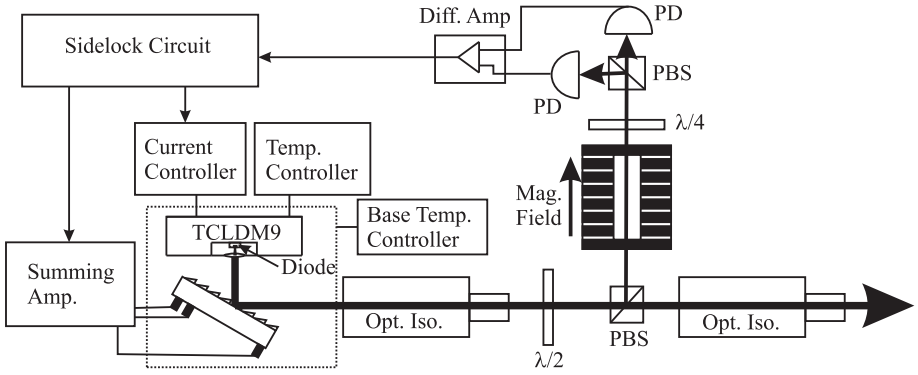

Figure 3.4: Schematic of the DAVLL setup and associated locking circuitry.

coarse adjustment, piezoelectric transducers (PZTs) are used to adjust the position of the grating for optimal feedback.

The diode laser and external cavity are supported by an aluminum plate. The temperature of the plate is controlled separately from the diode by a commercial temperature controller (Wavelength Electronics MPT2500) attached to three thermoelectric coolers (Thorlabs TEC3-2.5), monitored using a 10 kΩ thermistor (ThorLabs TH10K). The diode laser assembly is mounted atop a $6 \times 6 \times 6$ inch aluminum block that rests on sorbothane pads to isolate the laser from vibrations of the optics table. The entire mount plus laser is contained in an insulated enclosure. The enclosure consists of an outer layer of 1/4 inch plexiglass, 3/4 inch styrofoam, aluminum foil and an inner layer of 1/8 inch plexiglass. The outer layer acts as a acoustic reflector followed by an absorber. The layer of aluminum foil is attached to the optics table to electrically shield the laser. The enclosure also serves to isolate the laser from temperature fluctuations in the lab. The laser light passes through an anti-reflection coated window at near infrared wavelengths.

The light from the laser passes through an optical isolator and a small fraction ($\sim$ 5 %) is sent to a dichroic atomic vapor laser lock (DAVLL) spectrometer to frequency stabilize the diode laser. A weak beam of linearly polarized light is passed through a pyrex Cs vapor cell contained in a constant magnetic field (125 Gauss) generated by permanent ring magnets. The light is then passed through a quarter wave retarder

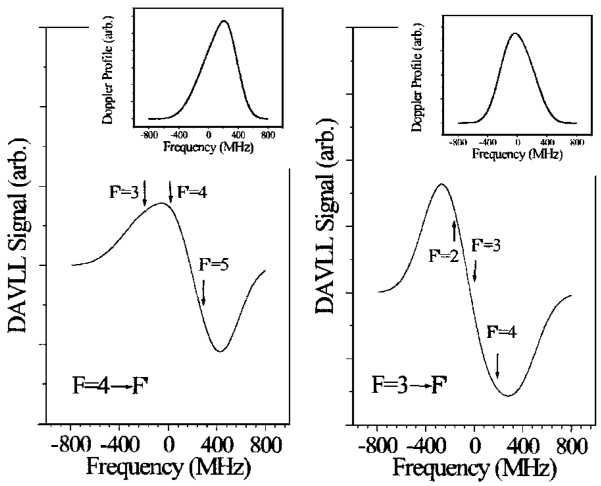

Figure 3.5: Dispersive curves for the (a) $F = 4 \rightarrow 5$ trapping transition and (b) $F = 3 \rightarrow 4$ repumping transition that acts as an error signal for locking.

and split using a polarizing beam splitting cube. The two beams are then monitored using two photodiodes.

The DAVLL is used to generate a dispersive curve (see fig. 3.5) that can be used as a frequency reference to lock the diode laser. The frequency of the transitions between magnetic sublevels will be shifted by the Zeeman effect. Linear polarized light is composed of a superposition of left and right circularly polarized light. By placing the gas in a magnetic field, the center frequency of absorption of the different circular polarizations will be shifted higher and lower in frequency due to selection rules on the Δm transitions of the most Zeeman shifted states. The quarter wave retarder rotates the circularly polarized components of the absorption signal to orthogonal linear components so that the two polarizations can be independently monitored on a photodiode after the polarizing beam splitter. The two signals can then be subtracted using a differential amplifier and an error signal is obtained.

Sample dispersive signals from a differential amplifier can be seen in fig. 3.6. The angle of the quarter wave retarder can be used to adjust the shape of the DAVLL signal. This signal is used to monitor the frequency of the laser and by unbalancing the light on the photodiodes, the center frequency and slope can be adjusted. The

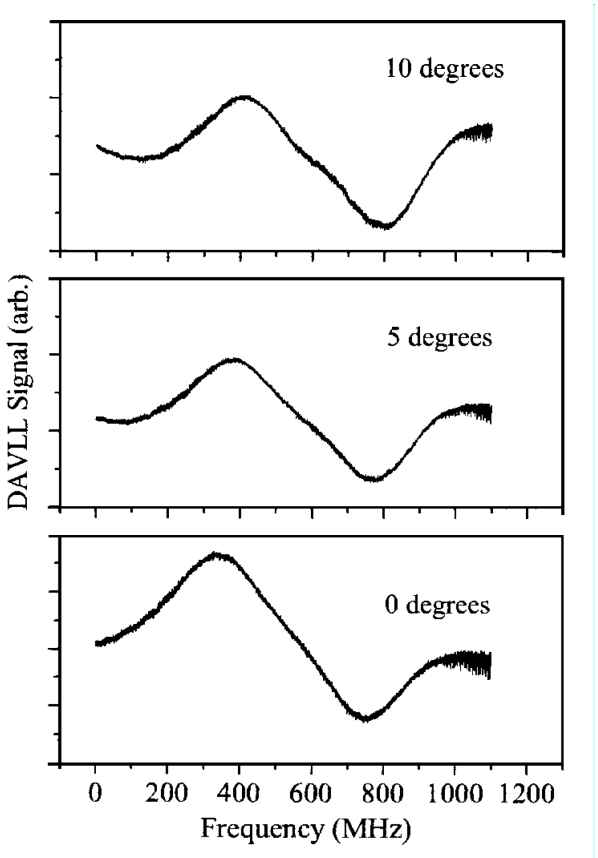

Figure 3.6: Experimental DAVLL traces for different quarter wave retarder settings. This figure illustrates that the DAVLL trace can be adjusted by unbalancing the light on the photodiodes.

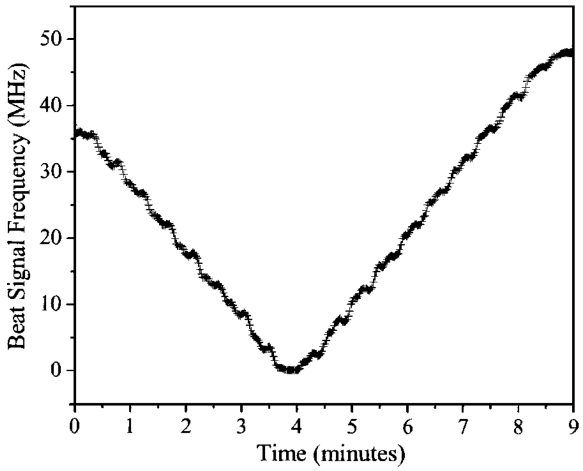

Figure 3.7: Measurement of the free running drift of the diode lasers by measuring the frequency difference between one frequency stabilized laser and one that is unstabilized.

trace is obtained by rapidly sweeping a voltage that is applied to the PZTs mounted behind the diffraction grating. This adjusts the cavity length and therefore tunes the laser. The traces here are scanned over a range $> 1\,\mathrm{GHz}$.

The DAVLL signal is input to a custom side-lock circuit obtained from JILA. The error signal is summed with a DC offset that sets the locking frequency of the laser on the DAVLL dispersion curve. Feedback is then applied using a proportional and integral gain controller to lock the frequency of the laser. Feedback is applied to both the PZTs and the diode current.

The DAVLL signal is split electronically into two components. One component is high frequency and the other is low frequency. The low frequency component spans the spectral region from DC to $\sim 1\,\mathrm{kHz}$ while the high frequency signal spans the spectrum from 1 to $\sim 2\,\mathrm{kHz}$. The low frequency error signal is passed through an adjustable gain amplifier and an integrator to the PZTs that control the grating position. The high frequency component of the error signal passes through a separate adjustable gain amplifier and an integrator. The high frequency error signal is fed back to the laser diode current controller.

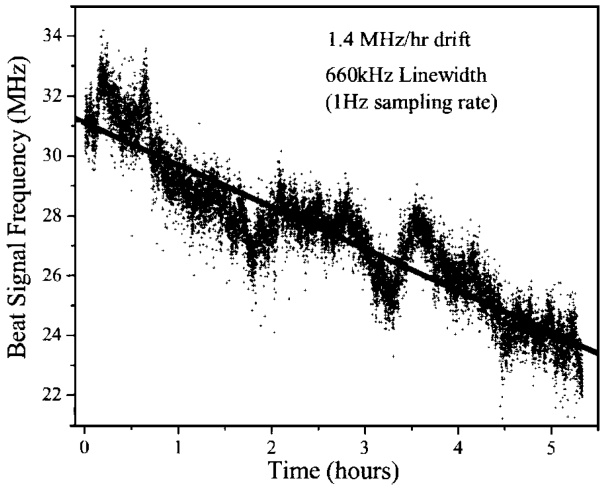

Figure 3.8: Long term relative frequency drift by monitoring the difference frequency for the two laser systems over an 8 h period.

The instantaneous linewidth was measured to be 200 kHz. The diffracted spot was shifted from the main beam by 58 MHz. The single laser beat signal was observed on a fast oscilloscope by Fourier transforming the amplified output from the fast photodiode. The 200 kHz linewidth is the deconvoluted FWHM assuming a Lorentzian line shape. The stability of the rf that powered the acousto-optic modulator was $\ll .2$ MHz. The drift of the free running laser was measured by recording a beat signal between one actively stabilized system and one system that was free running. A typical curve is shown in Fig. 3.7. The free running drift for the laser system was determined to be < 20 MHz/min on a ~ 10 min time scale.

To measure the long term drift and effective linewidth when the DAVLL lock was activated, two laser systems were detuned from each other by ~ 30 MHz and a beat signal was recorded. The amplified beat signal was fed into a frequency counter (EG&G 974) and recorded every 1.5 s for ~ 5 h. The counting time was 1 s. The results from a typical day are shown in Fig. 3.8. The long-term relative drift between the two laser systems was 1.4 MHz/h or 700 kHz/h average. The effective linewidth was 500 kHz over this same time period. The effective linewidth was taken to be the standard deviation from the laser drift deconvoluted assuming a Lorentzian line

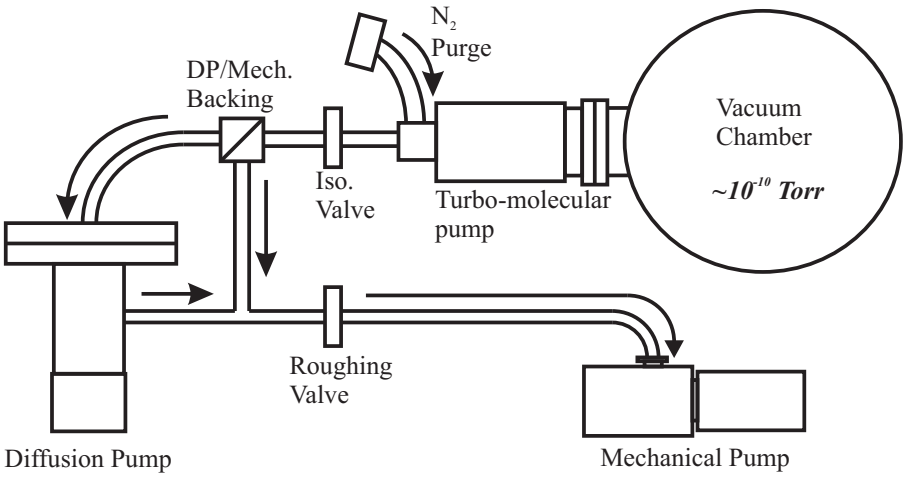

Figure 3.9: Diagram of the vacuum system.

shape. The values agree well with measurements of the stability of diode laser systems operating at wavelengths near 780 nm without temperature stabilization of the DAVLL spectrometer [26, 27]. A similar measurement was done by observing the Fourier transform of the beat signal on a fast oscilloscope. The signal indicated a linewidth of 500 kHz, consistent with that obtained from the beat signal record.

3.3 Vacuum System and Spectrometer

The photofragment time-of-flight spectrometer is contained in a 22.9 cm radius stainless steel vacuum chamber (see fig. 3.9). It is evacuated to a pressure of 2×10^{-10} Torr by a turbo-molecular pump. The turbo-molecular pump is backed by a diffusion pump which is backed by a mechanical roughing pump.

The vacuum system is designed to prevent contamination of the inside surfaces in the event of power failure. All systems are connected to a battery backup and are interlocked by a programmable logic controller (PLC).

The Cs MOT is formed in the center of the chamber. The MOT is formed using the two diode lasers described in the previous section and a set of anti-Helmholtz coils. One diode laser acts as the trapping laser and is detuned from the $6S_{1/2}(F =$

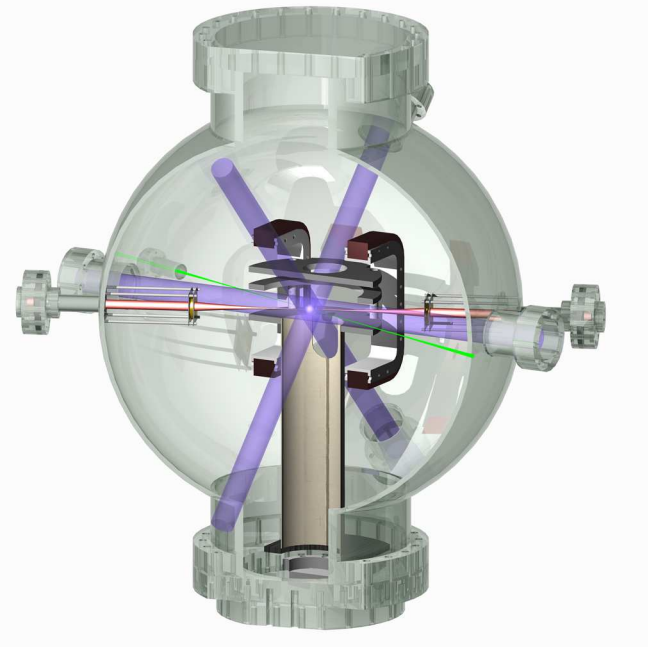

Figure 3.10: To scale rendering of the spectrometer located in the vacuum chamber. The spectrometer is sectioned for viewing. The bright spot in the center represents the MOT. The spectrometer is formed around the MOT with the flight tube extending downward towards the MCP detector. The anti-Helmholz coils are also depicted. The lens systems are used to focus a CO_2 laser to form an optical dipole trap.

4) $\rightarrow 6P_{3/2}(F' = 5)$ transition to provide cooling. The second diode laser acts as a repumping laser and is tuned to the $6S_{1/2}(F = 3) \rightarrow 6P_{3/2}(F' = 4)$ transition. This laser prevents population from building up in the $6S_{1/2}(F = 3)$ due to off-resonant population of the $6P_{3/2}(F' = 4)$ state. Rydberg atoms are excited by a Coherent 699-21 with a linewidth of $\sim 1\,\text{MHz}$ at $508 - 509\,\text{nm}$.

The anti-Helmholz coils for the MOT are located inside the chamber (see fig. 3.10). The coils are square with a length of 14.7 cm on a side. The coils contain 24 wrappings each of Kapton coated, copper tubing. Water is circulated through the coils to dissipate heat. The coils are operated at 34 A for a magnetic field gradient of 12.5 G/cm at the MOT along the direction coaxial with the anti-Helmholz coils.

The spectrometer is centered on the MOT. Three stainless steel, circular field shaping plates are distributed above and below the MOT. 33 mm above the MOT is a plate with holes for two of the MOT trapping beams. The holes are filled with

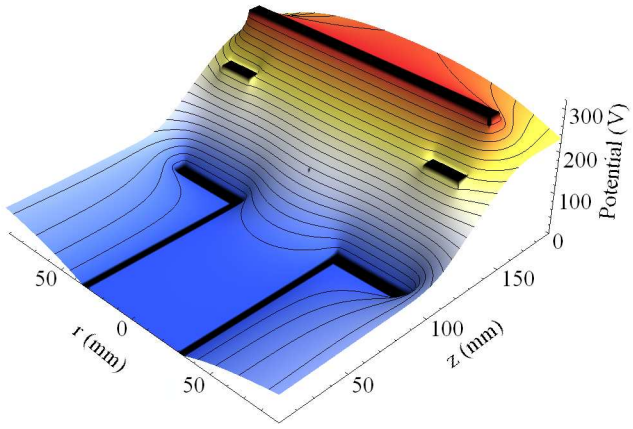

Figure 3.11: Plot of the equipotential surfaces with an applied voltage of 320 V on the top plate. The lensing of the field is due to the absence of a grid on the opening of the bottom plate. The MOT is displayed as a Gaussian distribution at its location on the surface.

glass and covered with an electro formed Ni wire mesh (4.6 lines/mm) on the side of the glass closest to the MOT. 19 mm below this plate is a field shaping ring. 28 mm below the shaping ring is a grounded plate with a 74 mm diameter hole. The MOT is located halfway between the bottom plate and the shaping ring. All three plates are separated by ceramic spacers. Connected to the bottom plate is a 25.4 cm grounded flight tube. The spectrometer is coated with Aerodag to minimize reflections and smooth out field imperfections. At the end of the flight tube is a 40 mm Z-stack cross delay-line (XDL) microchannel plate (MCP) detector (Sensor Sciences) with a 19 μm resolution determined from spot size measurements of a pinhole mask illuminated with ultraviolet light.

The Rydberg atoms are ionized and projected onto the detector by applying a high voltage pulse to the top plate. The pulse ionizes the Rydberg atoms and transfers a momentum kick, $p = \int qE(t)dt$ to the ions in the MOT region. q is the charge and E the electric field pulse as a function of time. The pulse is applied using a HV pulser (DEI PVX-4140) powered by a high voltage supply (Glassman EK3R200). Resistors are symmetrically spaced around the edges of the plates. The resistance between the top plate and shaping ring is 1 kΩ (4 resistors), and 2.1 kΩ between the shaping ring

and bottom plate (4 resistors) for a combined resistance of 3.1 kΩ. With an applied voltage of 320 V, there is an electric field of 53 V/cm at the position of the MOT. The rise time of the pulse is 80 ns limited by the HV pulser. The fastest rise time achievable is 10 ns, determined using a digital delay generator (SRS DG535). After the pulse, ions travel through the field free flight tube and are detected on the MCP.

Fig. 3.11 shows the calculated electric equipotential lines in the region around the MOT, for an applied voltage of 320 V. The potential is calculated by numerically solving the Laplace-equation in cylindrical symmetric 3D space using the program SIMION [29]. The symmetry axis coincides with the center of the flight tube. The cross section of the electrode configuration is specified on a 2D grid of 400 horizontal points by 200 vertical points with a grid spacing of 1 mm. The modeled electrodes match the spectrometer plate geometry. The top plate, the shaping ring, and the bottom plate and flight tube are modeled as ideal conductors at fixed potentials of 320 V, 218 V, and 0 V, respectively. No other parts of the experimental setup are included in the simulation. Under these conditions, the longitudinal electric field at the MOT is calculated to be $\epsilon_l = 52.2\,\mathrm{V/cm}$. The field gradient of $\partial\epsilon_l/\partial z = 8.87\,\mathrm{V/cm^2}$ at the MOT center implies that the field changes by 92 mV/cm over the 100 μm extent of the excitation volume in the time-of-flight direction. The radial electric field gradient at the MOT is $\partial\epsilon_r/\partial r = 4.23\,\mathrm{V/cm^2}$. We assume no stray electric field for the simulation. From the calculated field at the MOT, we obtain a geometric factor $\alpha_t = \epsilon/V_0 = 1.63 \times 10^{-1}\,\mathrm{cm^{-1}}$ relating the applied voltage and the field at the MOT position.

Time-of-flight velocity distributions can be reconstructed using high speed electronics (see fig. 3.12). The current monitor of the HV pulser is processed using a constant fraction discriminator (CFD) and serves as the start input for a 2 GHz multichannel analyzer (MCA) (Fast ComTec P7886). Fast timing signals (FWHM $\sim$ 2 ns) from the MCP anode are amplified using a preamplifier (SR240). The am-

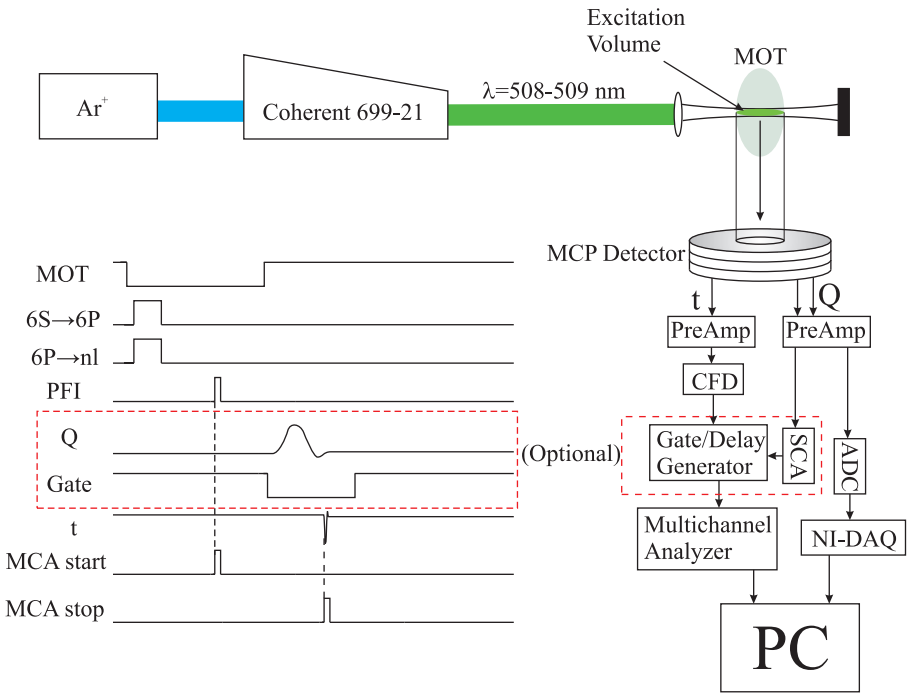

Figure 3.12: Timing diagram and experimental setup for measuring TOF distributions. The dashed region can be included if charge discrimination is desired. The fast timing signals from the anode of the detector are amplified by a fast preamp and discriminated using a CFD. The timing signals pass through a delay generator that can be gated using an SCA that discrimates based on the charge Q. The charge released by the MCP can be measured using an analog-to-digital converter (ADC). The edge of the PFI serves as the start pulse for the multichannel analyzer while the fast timing signals serve as the stop.

plified signals are processed using a second CFD and serve as stop inputs for the MCA. The XDL grid beneath the MCP is designed for 2D imaging of product spatial distributions. The signals from the XDL grid are integrated by preamplifiers (Sensor Science) for 3 μs to provide a charge signal proportional to the number of ions incident on the detector. The fast timing signals can be filtered using the charge signals [28]. The charge signals may be used to gate the fast timing signals by using a single channel analyzer to threshold the velocity distributions based on the height of the charge pulse [28]. The charge pulse height distribution (PHD) is also read by an analog to digital converter (Sensor Science OMNI ADC). The charge PHD is determined by the binomial distribution and is a measure of the overall detection probability of the system if the number of products in a collision is known [14].

We measured the lifetime of the 133D state to characterize the blackbody decay rate of the Rydberg atoms created in our spectrometer. From the expression given by Farley and Wing [20] we predict $\tau_{bb} = 900\,\mu$s (see Chap. 2). We then expect $\tau_{eff} = 560\,\mu$s for the Cs $133D$ state.

We measured τ_{eff} of the $133D$ state to compare with the predicted value. The $133D$ state was excited from the MOT $6P_{3/2}(F' = 5)$ state using the dye laser at $\lambda \sim 508.45\,$nm. We stepped the PFI pulse by 50 μs steps using a programmable digital delay generator (THORLabs DG100N). The experiment was conducted at 500 Hz with a 70 V PFI pulse at low dye laser intensity. The laser intensity was kept low ($< 1\,$Hz) to avoid spontaneous ionization effects [51].

The measurement of τ_{eff} for the $133D$ state can be seen in fig. 3.13. The data fit to an exponential decay gives $\tau_{eff} = 580 \pm 60\,\mu$s. This is in good agreement with the predicted value of $\tau_{eff} = 560\,\mu$s. The long lifetime of Rydberg atoms is ideal for use in Rydberg tagging of photofragments. Atoms can be allowed to expand as neutrals rather than ions for increased energy resolution in ultracold collisions.

A small stray electric field is present in our experimental setup. Fig. 3.14 shows

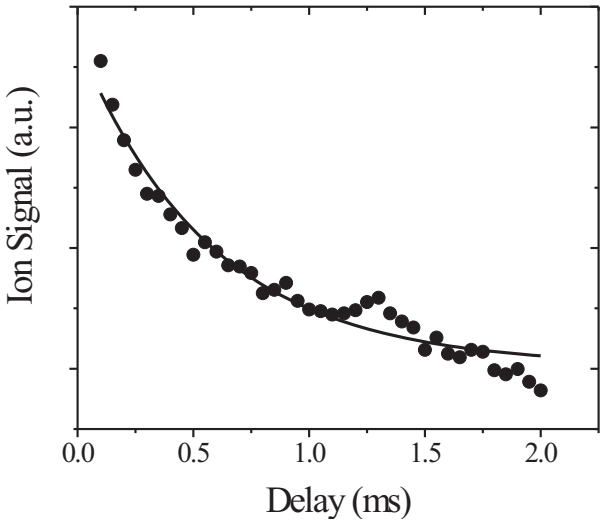

Figure 3.13: Measurement of ion yield as a function of PFI delay. The red line is the fit to a 1st order exponential decay with an effective lifetime $\tau_{eff} = 580 \pm 60\,\mu$s.

the experimental dependence on the the $121P$ and $120D$ states of Cs. The excitation of the P state is due to the mixing induced by a stray electric field. It is important to fully characterize this field to properly explain the dynamics of the Rydberg interactions.

To measure the stray field at the position of the MOT, we measured the spectrum of the $120D$ Rydberg level. The $120D$ state was chosen because of the sensitivity of high principle quantum number Rydberg states to electric fields. The splitting between the $j = 3/2, m_j = 3/2$ and $j = 5/2, m_j = 1/2$ was used to probe the background field by varying the magnitude of an applied electric field during excitation.

The applied field was varied between 1 and $-46\,$mV/cm to measure the stray electric field by applying a constant voltage to the top plate of the spectrometer. The DC Stark shift will cause the m_j states of the Rydberg levels to be split in the applied electric field. At zero field, the splitting between the $120D_{3/2}$ and $120D_{5/2}$ fine structure states is predicted to be 37MHz using the quantum defects and fine structure splitting from [31, 32]. The experimental results of the measurement of the stray electric field are given in fig. 3.15. With no applied background field, we find the

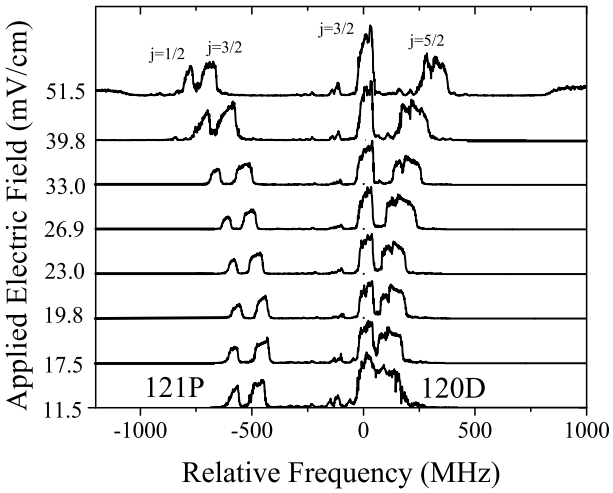

Figure 3.14: Spectra taken for the $121P$ and $120D$ states of Cs at different applied electric fields. At the highest field shown, the $l > 2$ Stark fans are visible to the left and right of the P and D states. As can be seen, small changes in field strength create large frequency shifts at high n.

fine structure levels to be Stark shifted with a splitting between the $j = 3/2, m_j = 3/2$ and $j = 5/2, m_j = 1/2$ states to be 131 MHz. This splitting is consistent with a stray field of 17 ± 1 mV/cm [21, 30]. By applying a negative voltage to the top plate of the spectrometer during excitation, we were able to minimize the splitting of the Rydberg levels with an applied field of 8 ± 1 mV/cm. There is a residual stray electric field perpendicular to the applied field of 15 ± 1 mV/cm which causes a minimum splitting of 123 ± 2 MHz. Fitting the Stark shift calculation to the experimental values is consistent with prior measurements of the $89D$ and $66D$ states fit with the same method. The splitting is checked periodically to ensure that the experimental conditions have not changed between measurements.

3.4 Density Dependent Effects: Multiple Photon Scattering

The following section describes experiments that were performed to analyze the atom number and density distribution in the MOT. The density distribution was analyzed using computed tomography through the inverse Abel transform to reconstruct the

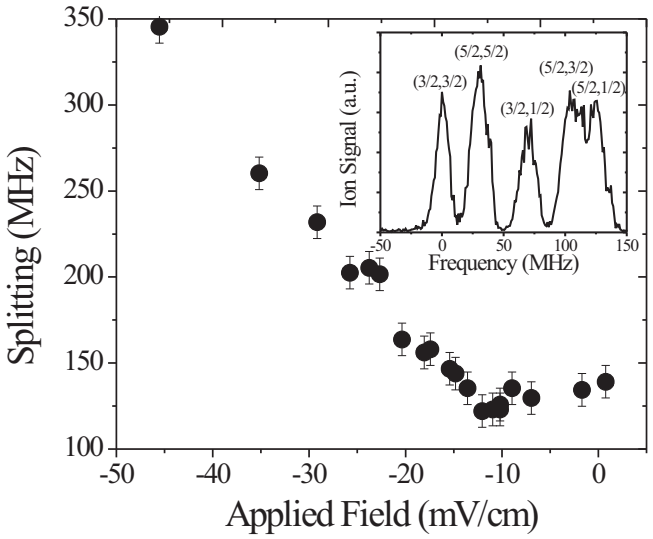

Figure 3.15: Measurement of the stray electric field present in the chamber at the position of the MOT. The minimum in the measurement gives the component of the field that is perpendicular to the time-of-flight axis.

3D density distribution from a 2D projection. Two methods were used, each with similar results. The Abel inversion was used to study the onset of multiple photon scattering in the MOT which occurs at high densities.

Many semi-empirical models have been introduced to predict the behavior of the MOT [25, 33]. One early model was based on the multiple scattering of photons [33]. The model predicted that the MOT density becomes uniform, yielding a flat-topped intensity projection instead of a Gaussian one at high atom number, $\sim 10^5$. The effect is a consequence of the repulsive force that results from the radiation pressure due to multiple photon scattering. Signatures of multiple scattering were observed in later studies, but at different atom number [25, 34–37]. In some of these studies, the intensity projection of the MOT was observed and it did not deviate from Gaussian [25, 34]. Whether or not the density distribution of the MOT becomes constant in the multiple scattering regime is an outstanding question that can provide experimental insight into the light pressure forces that determine the behavior of the MOT.

Measuring the density of laser atom traps is difficult but important to many

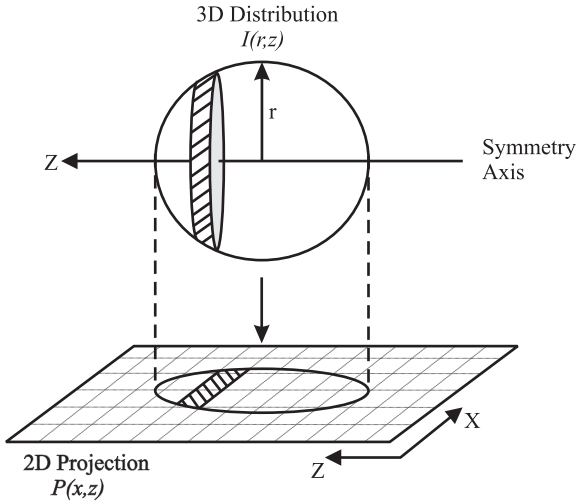

Figure 3.16: Illustration of the mapping of a 3D distribution onto a 2D plane.

experiments, particularly those involving collisions between cold atoms. Techniques for analyzing MOT properties, such as peak density and volume, rely on digital images taken of the MOT fluorescence or absorption imaging. The images are 2-D projections of 3-D distributions (see fig. 3.16).

3-D distributions can be reconstructed from 2-D projections using computed tomography. We show that the 3-D density distribution of the MOT can be recovered using the Abel transformation from CCD images of MOT fluorescence. The Abel transform is appropriate for this task because the magnetic field used for the MOT is axially symmetric. Our method is a non-destructive way to measure the density distribution of the MOT. The technique developed here to study the MOT can be used in a similar fashion to investigate other axially symmetric traps such as optical dipole traps.

There are many different approaches to calculating the Abel transform. Each method varies in complexity, computation time, and sensitivity to noise. We chose to use two methods, the Fourier-Hankel method [38] and the Gaussian basis-set expansion (BASEX) [39]. We find that both methods are useful and discuss the advantages and implementation of each one. Computed tomography requires only a CCD camera

to acquire the images. Most MOT experiments use a CCD to observe the MOT. If the response of the CCD array is calibrated, there is no need for a photo-multiplier tube (PMT) to determine the density distribution. The inversion can be done in real time, as fast as the acquisition rate of the camera.

3.4.1 Atom counting experiments

During the experiments, the MOT fluorescence is imaged onto a CCD array. The CCD array contains 1004×1004 pixels each with dimensions of $7.4\,\mu\text{m} \times 7.4\,\mu\text{m}$. The number of atoms in the trap is measured using a calibrated photomultiplier tube (PMT). The atom number N is found by measuring the light power P emitted from the MOT and dividing by the scattering rate

$$N = P/R \tag{3.6}$$

The emitted light power from the MOT is collected onto the calibrated PMT. Measurements of atom number using a PMT together with Abel inverted CCD images provide measurements of MOT density.

One signature of multiple scattering is a linear scaling of volume with atom number. In this regime, the density becomes constant. Our measurements indicate that multiple scattering occurs at a density of $n_{MS} = 2.15 \times 10^{10}$ for our Cs MOT. As can be seen in fig. 3.17, the density increases linearly with atom number until n_{MS} is achieved. The abrupt change from the temperature limited MOT to the multiple scattering regime is clearly visible.

A plot of volume versus atom number is shown in fig. 3.17(b). It can be seen that the volume is constant until the atom number reaches a value $N_{MS} = 2.7 \times 10^6$. At this atom number, the volume grows linearly. The linear growth of the volume is the signature of multiple scattering. The radius of the MOT in the multiple scattering

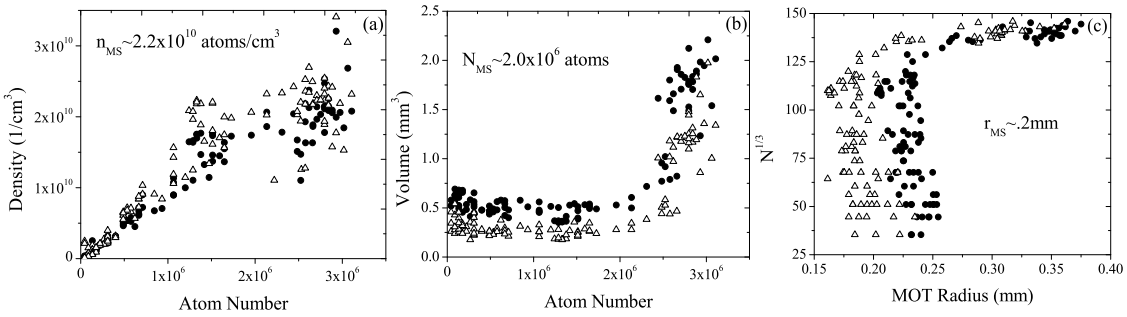

Figure 3.17: Measurements of the (a) peak density vs. atom number, (b) volume vs. atom number, and (c) Cubed root of the atom number vs. MOT radius.

regime is [25]

$$r_{MS} = \frac{1}{\sqrt{2\pi}} \left(\frac{N}{n_{MS}} \right)^{1/3} \tag{3.7}$$

The density and atom number can be combined to verify the minimum value of the multiple scattering radius $r_{MS} = .2\,\text{mm}$ (fig. 3.17(c)).

Other work has predicted that the MOT radius will scale as $N^{1/3}$ in the multiple scattering regime [40]. The $N^{1/3}$ scaling was observed experimentally for Rb [37]. We also observe a $N^{1/3}$ dependence on MOT radius in fig. 3.17(c). Multiple scattering occurs for $N^{1/3} > 125$ in our work with a Cs MOT. This value agrees well with other experiments on Cs [35].

3.4.2 Density Measurements through Abel Inversion

The density distribution of the MOT is recovered from images of fluorescence obtained with the CCD array. A CCD image is the 2D projection of a 3D density distribution as depicted in fig. 3.16. In cases with axial symmetry, the 3D distribution can be reduced to two dimensions by the replacement

$$r = \sqrt{x^2 + y^2} \tag{3.8}$$

The 3D density distribution is represented by a function $I(r, z)$. $I(r, z)$ is cylindrically symmetric so the θ coordinate is omitted. The 2D projection of $I(r, z)$ is

$$P(x, z) = 2 \int_x^\infty \frac{I(r, z) r}{\sqrt{r^2 - x^2}} dr \tag{3.9}$$

where x is the distance from the symmetry axis in projection space. For the Abel transform, each value of z in the projection is treated independently. The 3D distribution $I(r, z)$ can be recovered from the 2D mapping $P(x, z)$ by using the inverse Abel transform [41],

$$I(r, z) = -\frac{1}{\pi} \int_r^\infty \frac{dP(x, z)/dx}{\sqrt{x^2 - r^2}} dx \tag{3.10}$$

To implement the inverse Abel transform to recover $I(r, z)$, a numerical algorithm is required. The primary difficulties in implementing a numerical algorithm to evaluate eqn. 3.10 are the derivative and the singularity in x. The derivative $dP(x, z)/dx$ causes numerical difficulties when the image to be inverted has sharp features or contains excessive noise. Sharp features and noise from the experiment can cause the derivative to diverge, giving inaccurate results. The derivative requires smoothing and filtering of the data in any practical analysis using the Abel inversion.

Routines for symmetrizing and smoothing experimental data for inversion have been developed [38, 42, 43]. A common technique is to treat one line of pixels perpendicular to the symmetry axis of the 2D projection. One line of pixels for constant z is referred to as a "slice" of the image. One slice of the distribution and its projection are depicted in fig. 3.16.

Fourier analysis can be applied to symmetrize the projection. Axial symmetry in the 3D distribution implies that the Fourier components of the 2D projection should be real and even about the symmetry axis. Removal of the imaginary components leaves a symmetric projection.

Abel inversion requires axial symmetry, but it can be a challenge to properly iden-

tify the axis of symmetry. The symmetry axis of the projected distribution can be ill defined due to noise. For a MOT, beam misalignment, beam shape and beam intensity imbalances predominantly contribute to asymmetry. Blurring algorithms have been developed and implemented for particularly noisy data to help find the symmetry axis [42, 43]. We did not find a need for blurring techniques in our experiments; however, great care was taken to ensure a symmetric MOT.

3.4.3 Fourier-Hankel Transform method

The Fourier-Hankel method has been successfully applied to ion imaging [42]. The Fourier-Hankel method starts by performing a Fast-Fourier Transform(FFT) of each slice. In Fourier-Space, the image is filtered and re-centered using the algorithm outlined in [38]. Symmetrization and smoothing are followed by a discrete, inverse Hankel-Transform to recover the 3D distribution.

We can recover the distribution $I(r)$ from its projection $P(x)$ by considering the Fourier transform of $P(x)$ in polar coordinates. The Fourier transform of $P(x)$ is

$$F\left\{P(x)\right\} = \int_{-\infty}^{\infty}\int_{-\infty}^{\infty} I\left(\sqrt{x^2+y^2}\right) e^{-2\pi i x k} dx dy \tag{3.11}$$

Transforming to polar coordinates allows 3.11 to be written

$$F\left\{P(x)\right\} = \int_{0}^{\infty}\int_{0}^{2\pi} I\left(r\right) e^{-2\pi i k r\cos\theta} r d\theta dr \tag{3.12}$$

The zero-order Bessel function

$$J_0(2\pi k r) = \frac{1}{2\pi}\int_{0}^{2\pi} e^{-2\pi i k r\cos\theta} d\theta \tag{3.13}$$

can be substituted to yield

$$F\{P(x)\} = 2\pi \int_0^\infty rI(r)J_0(2\pi kr)dr \tag{3.14}$$

Eqn. 3.14 is the zero-order Hankel transform of $I(r)$. Because the zero-order Hankel transform is identical to its inverse [41], we can recover $I(r)$ using,

$$I(r) = 2\pi \int_0^\infty kJ_0(2\pi kr) \int_{-\infty}^\infty P(x)e^{-2\pi ixk}dxdk \tag{3.15}$$

The integral over dx is accomplished numerically using a FFT. The real part of the transformed projection is then symmetrized and smoothed (see ref. [38]). Finally, the inverse Hankel transform is applied to recover the distribution $I(r)$. This procedure is repeated for each slice of the image along z (see fig. 3.16).

3.4.4 Gaussian basis-set expansion (BASEX) Abel Transform method

The BASEX method is an alternative to the Fourier-Hankel method [39]. In situations where the projection is high resolution or has a large dynamic range, the BASEX method can be more efficient than the Fourier-Hankel method. The essential feature of the BASEX method is an expansion of the projection in a set of functions that have analytic Abel inversions.

The BASEX method can be understood if we recognize that the Abel transform is a linear operation. The projection $P(x, z)$ is the Abel transform of $I(r, z)$

$$P(x, z) = Abel\{I(r, z)\} \tag{3.16}$$

If we expand the distribution $I(r,z)$ in terms of N basis functions, $f_k(r,z)$,

$$I(r,z) = \sum_{k=0}^{N-1} C_k f_k(r,z) \tag{3.17}$$

where the C_k are expansion coefficients. The projection can be expressed as

$$P(x,z) = \sum_{k=0}^{N-1} C_k Abel\left\{f_k(r,z)\right\} = \sum_{k=0}^{N-1} C_k G_k(x,z) \tag{3.18}$$

The functions $G_k(x,z)$ are the Abel transform of the basis functions $f_k(r,z)$. It is advantageous to choose the basis functions to have analytic Abel inversions. This choice avoids the noise problems (derivative and singularity) that occur when evaluating the Abel inversion numerically. The basis can also be chosen to assume rapid convergence of the $I(r,z)$ expansion.

The method then reduces to determining the coefficients C_k. Calculation of the C_k is most easily accomplished using matrix algebra. The method is summarized as follows. The CCD image is symmetrized and filtered in Fourier space and then returned to projection space. Next the projection is expanded in a basis of Abel transformed functions for each slice to determine the C_k. Finally, the expansion coefficients are used to reconstruct the density distribution.

3.4.5 Calculation of Expansion Coefficients

If we let $i = 1$ to N_x and $j = 1$ to N_z where $N_x \times N_z$ is the number of pixels in the projection, we can cast the projection as a matrix multiplication

$$\mathbf{P}_{ij} = \sum_{k=0}^{K-1} \mathbf{C}_k \mathbf{G}_{ij}^{(k)} \tag{3.19}$$

or more compactly

$$\mathbf{P} = \mathbf{CG} \tag{3.20}$$

The Abel transform of the basis functions is

$$\mathbf{G}_{ij}^{(k)} = 2 \int h(x - x_i, z - z_j) dx dz \int_x^\infty \frac{r f_k(r, z)}{\sqrt{r^2 - x^2}} dr \tag{3.21}$$

where (x_i, z_j) are the pixel coordinates in the projection space [39]. The function $h(x - x_i, z - z_j)$ is determined by experiment. It is an instrumental weight that can be set equal to a delta function if no instrumental weighting or smoothing is needed. We used

$$h(x - x_i, z - z_j) = \delta(x - x_i)\delta(z - z_j) \tag{3.22}$$

where (x_i, z_j) is the pixel coordinate on the CCD image.

For axial symmetric distributions, $f_k(r, z)$ is separable

$$f_k(r, z) = \rho_m(r)\xi_n(z) \tag{3.23}$$

The separability of $f_k(r, z)$ makes it convenient to define

$$\mathbf{X}_{mi} = 2 \int h_x(x - x_i) dx \int_x^\infty \frac{r \rho_m(r)}{\sqrt{r^2 - x^2}} dr \tag{3.24}$$

and

$$\mathbf{Z}_{nj} = \int h_z(z - z_j)\xi_n(z) dz \tag{3.25}$$

The definition of $\mathbf{Z}_{nj}$ allows us to determine $\mathbf{X}_{mi}$ for a fixed z. This is analogous to treating a slice in z in the Fourier-Hankel method. The 2D projection is

$$\mathbf{P}_{ij} = \sum_{m=0}^{N_x - 1} \sum_{n=0}^{N_z - 1} \mathbf{C}_{mn} \mathbf{X}^{mi} \mathbf{Z}_{nj} \tag{3.26}$$

or in matrix form

$$\mathbf{P} = \mathbf{X}^T \mathbf{C} \mathbf{Z} \tag{3.27}$$

Solving for $\mathbf{C}$ gives

$$\mathbf{C} = \mathbf{APB} \tag{3.28}$$

where,

$$\mathbf{A} = (\mathbf{X}\mathbf{X}^T + \lambda_x \mathbf{I})^{-1}\mathbf{X} \tag{3.29}$$

and

$$\mathbf{B} = \mathbf{Z}^T(\mathbf{Z}\mathbf{Z}^T + \lambda_z \mathbf{I})^{-1} \tag{3.30}$$

λ_x and λ_z are the regularization parameters for $\mathbf{X}$ and $\mathbf{Z}$ respectively. Regularization is necessary if the basis functions $\rho_m(r)$ and $\xi_n(z)$ under or over-determine the matrices $\mathbf{X}$ and $\mathbf{Z}$. Regularization keeps $\mathbf{A}$ and $\mathbf{B}$ from becoming singular in a numerical calculation. The process used above is known as Tikhonov regularization [44].

The basis function $\rho_m(r)$ should be analytically integrable and smooth to take advantage of the BASEX method. For these reasons, we chose

$$\rho_m(r) = \left(\frac{e}{m^2}\right)^{m^2} \left(\frac{r}{\sigma}\right)^{2m^2} e^{-(r/\sigma)^2} \tag{3.31}$$

where σ is equal to the pixel size. If $h(x - x_i) = \delta(x - x_i)$ (no instrumental weighting) we can integrate $\mathbf{X}_{mi}$ to obtain

$$\mathbf{X}_{mi} = 2\sigma\rho_m(x_i)$$

$$\times \left[1 + \sum_{l=1}^{m^2} \left(\frac{x_i}{\sigma}\right)^{-2l} \prod_{q=1}^{l} \frac{(m^2 + 1 - q)(q - 1/2)}{q}\right] \tag{3.32}$$

Similarly, $\xi(z_j) = \rho_n(z_j)$ simplifies the problem.

In our calculations, we selected the number of basis functions to be half the number of pixels in each dimension of the image so that our matrices were well conditioned. The images were filtered and symmetrized in Fourier-space as in the Fourier-Hankel method. The images were returned to real space, and the BASEX method was used

to obtain $I(r, z)$.

3.4.6 Comparison of Methods

We compared both transform methods. The images were centered and symmetrized the same way for both transform methods [38]. We applied a Butterworth filter in Fourier space in each of the transform routines. The Butterworth filter is

$$B(k) = \frac{1}{1 + \left(\frac{k}{k_0}\right)^{2n}} \tag{3.33}$$

k is the spatial frequency in units of inverse length. k_0 sets the cut-off frequency and n is the order of the filter. The order sets the sharpness of the cutoff. We took great care not to over filter the data in our experiments. Because the MOT is $\sim 1\,\mathrm{mm}$ in size, k_0 determines how many spatial frequencies will be used to reconstruct the distribution. For the Fourier-Hankel method, we set $k_0 = 7\,\mathrm{mm}^{-1}$ with order $n = 15$. For the BASEX method, we set $k_0 = 20\,\mathrm{mm}^{-1}$ with order $n = 15$. k_0 is set smaller for the Fourier-Hankel method to avoid creation of artificial structures that would distort the data. Distortion can occur because of the derivative in the inverse Abel transform. Sharp features have divergent derivatives that can corrupt the transformed distribution. Over-filtering during the Fourier-Hankel method can also be detrimental as it would smooth the distribution to look more Gaussian. For a detailed treatment of filtering and symmetrizing routines, the reader is referred to [38]. The BASEX method is not as sensitive to the noise, allowing more frequencies to be retained. Keeping more frequencies allows finer structure to be visible. We used the inverted images from the BASEX method as a benchmark for the Fourier-Hankel method in some of the noisier images.

The differences between the inversion techniques can be seen in fig. 3.18. Fig. 3.18 shows a typical dataset viewed perpendicular to the symmetry axis. Both inversion

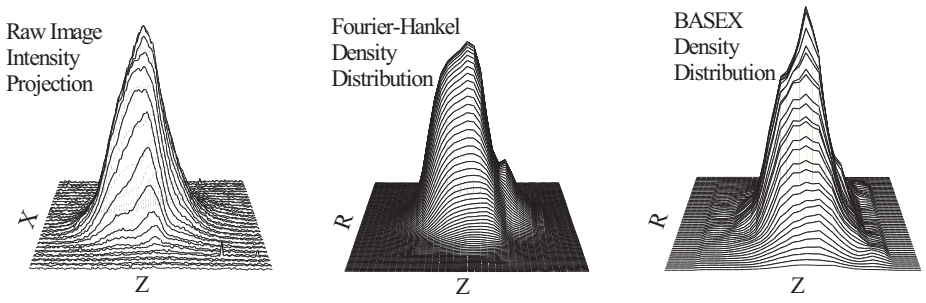

Figure 3.18: (a) Raw data processed using the (b) Fourier-Hankel method and (c) BASEX method.

methods show the existence of structure that is masked in the 2D projection. The density distribution is more clearly defined for the Abel Inversion. The Fourier-Hankel transform conveys less information about the spatial variations of the MOT due to the necessity of filtering with smaller bandwidth. For the BASEX method, the resolution of the CCD influences the size of the basis. Basis set computation can take considerable time. Once computed, the basis set can be reused to analyze images taken under the same experimental conditions.

A sample image can be seen in fig. 3.18. CCD images of fluorescence are commonly interpreted as a measurement of the density distribution. Interpreting the raw image as a distribution of density can lead to misleading results. A difficulty arises when deciding the extent of the distribution to be included as the volume. Whether to use the $1/e$ or $1/e^2$ radius of the distribution can lead to differences in reported volumes and densities. The Abel inversion methods return the density distribution of the raw image. The Abel inversion avoids the choice of the $1/e$ or $1/e^2$ radius when the image to be inverted contains a region of zero signal surrounding the distribution.

There is a slight difference in volume calculated using the two different inversion methods. The volumes we report are the peak densities divided by atom number. It can be seen in fig. 3.17 that the Fourier-Hankel method returns density distribu-

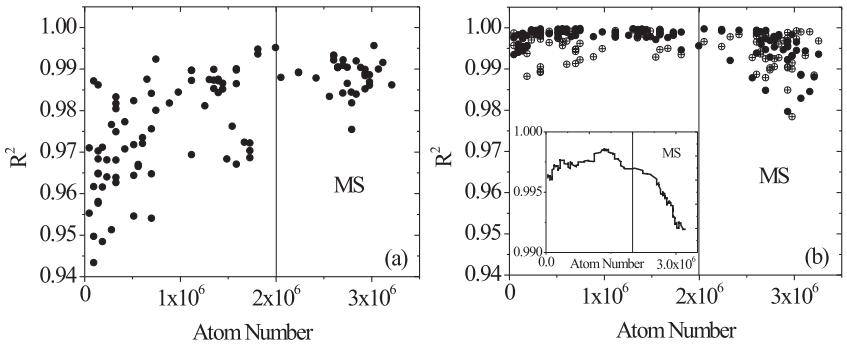

Figure 3.19: R^2 of a Gaussian fit vs. atom number. The decrease in the R^2 of the fit shows the onset of multiple scattering, i.e. where the distribution begins to deviate from Gaussian.

tions that indicate slightly larger volumes. This is most likely due to the additional smoothing in the Fourier-Hankel routine. The use of fewer spatial frequencies in the Fourier-Hankel method results in a broader distribution. The BASEX method includes higher frequency components that can more easily account for abrupt changes in the distribution. The lower components of the Fourier-Hankel method tend to smooth the sharp features and absorb them as additional volume.

It has been suggested in other work using a simple model that the distribution of the atoms in the MOT will resemble a flat-topped distribution in the multiple scattering regime [33]. A flat-topped distribution indicates a constant density when the Abel inversion algorithm is applied. We tested this by fitting a Gaussian to the raw images and Abel transformed images using the Levenberg-Marquardt non-linear least squares method. The r^2 value of a Gaussian fit is plotted against atom number in fig. 3.19. The two Abel inversion methods do show some departure from Gaussian in the multiple scattering regime. The departure is slight and is not evident in the raw images. This departure is evidence for a redistribution of density but the distribution was still strongly correlated to a Gaussian.

Correlation shows that the density distribution does not deviate significantly from a Gaussian in the presence of multiple scattering. We observed no evidence of a flat-

topped distribution in any of our measurements. All the images obtained were highly correlated with Gaussian distributions. These observations are consistent with other measurements where a flat-topped distribution was not observed [25, 34].

From this work it can be seen that the simple interpretation of the 2D projection as representing the 3D density distribution is insufficient for observing the onset of multiple scattering. Using the methods described for computing the inverse Abel transform, it should be possible to recover $I(r, z)$ in real time using high speed data acquisition with a CCD camera.

3.5 Summary

The prior sections describe the important parameters for the operation of the spectrometer. With measurements of atom number and CCD images, the density can be inferred. With the spectrometer design and diode laser construction, Cs atoms can be trapped and confined for measurements using time-of-flight velocity distributions.

Chapter 4

Temperature Measurements

In this chapter I will describe the technique developed in our laboratory for measuring the velocity of the atoms in the MOT using Rydberg tagging. I will explain how time-of-flight (TOF) velocity distributions were used to measure sub-doppler temperatures and measure the dependence of temperature on our experimental parameters. In these measurements, the expansion of the excited Rydberg atoms from an initial volume will be monitored as a function of delay between excitation and pulsed-field ionization. By testing the measurement using atoms from the MOT, the experiment can be calibrated and the ultimate velocity resolution can be established.

Rydberg tagging is an experimental technique for measuring product yield and product velocities that has been well established [45–48]. Rydberg tagging is excitation of an atom or molecule to a Rydberg state for the purpose of ionizing in a relatively weak field for ion detection. It has the advantage that after a collision process takes place, a product can be excited to a Rydberg state and expand as a neutral rather than an as an ion. Expansion as a neutral helps reduce the effects of unwanted, inhomogeneous stray electric fields on the angular distribution of and velocity of the products. Rydberg tagging has been proven effective at measuring velocities on the order of $\sim$cm/s [28].

In order to measure the small recoil velocities that result from Rydberg atom collisions, it is important to calibrate the velocity resolution of the spectrometer. This

calibration was performed by measuring the temperature of the MOT as a function of trapping laser parameters which results in a measurement of C_σ from eqn. 3.4. By comparing our measured value of C_σ to other published results, we have confidence that we understand the ion trajectory dynamics.

The temperature measurement is grounded in the assumption that nearly zero kinetic energy is transferred to trapped atoms upon excitation to an atomic Rydberg state. An atom in a Rydberg state will not remain trapped because it will not scatter the trapping photons during its long lifetime. The excited Rydberg will move at its thermal velocity and drift away from the initial excitation volume. By accumulating time-of-flight distributions as a function of delay, τ between excitation and pulsed field ionization (PFI), the temperature of the atoms in the MOT can be deduced. The recoil of the ion due to the ejected electron is negligible due to the much larger mass of the Cs^+ ion.

The experimental procedure is as follows. The light from the Coherent 699 dye laser is switched on with an AO for $1\,\mu$s. After a time $\tau = 50 - 400\,\mu$s, the PFI is applied at $53\,$V/cm for $4\,\mu$s. The PFI current monitor is input into a constant fraction discriminator and is used as the start input timing reference for the MCA. The PFI transfers a momentum kick $\Delta p = \int_0^{4\,\mu\text{s}} eE(z(t))dt$ to the ions which determines the time of flight to be $\sim 27\,\mu$s. The charge released by the detector after an ion impact is used to discriminate based on charge. The charge is input into a single channel analyzer and used to gate the fast timing signals. Only ion impacts that correspond to a single ion hit are processed with a constant fraction discriminator and counted by the MCA as a stop timing input. Measurements are repeated at a rate of $1\,$kHz until TOF distributions are accumulated as a function of τ.

The charge selection improves the resolution of the experiment by eliminating unwanted Coulomb broadening of the TOF distribution. If two atoms are excited, after PFI they will experience their mutual Coulomb fields and repel each other during

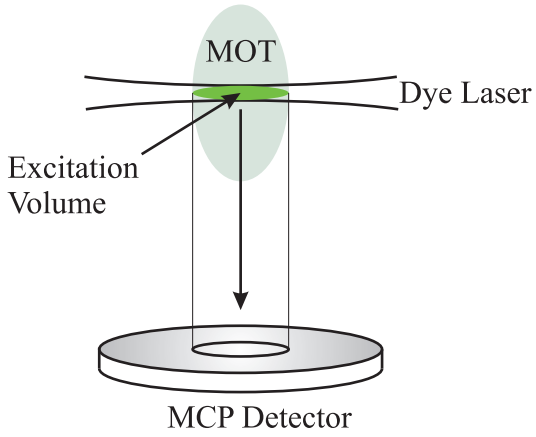

Figure 4.1: The laser intersects the MOT forming an excitation volume determined by the focus of the dye laser. The beam and MOT convolve to form a Gaussian shape excitation volume. The atoms are allowed to expand and are projected down towards the MCP detector.

the TOF. This will broaden the TOF distribution and cause the measurement of temperature to be systematically high. During the experiment, the dye laser intensity was kept low enough so that at an experimental rate of 1 kHz, the ion count rates were ~ 10 Hz. At these low rates, it is improbable that more than one ion was present during the TOF, with the charge discrimination as backup.

The width of the TOF distribution will depend on the initial width of the excitation volume and the temperature of the atoms in the MOT (see fig. 4.1). The dye laser that excites Rydberg states is focused through the MOT parallel to the detector surface. The thermal distribution of the atoms with FWHM Δi in the i direction is

$$f(\boldsymbol{r};\boldsymbol{v},\tau) \propto \prod_{i=x,y,z} e^{-(i-v_i\tau)^2 4ln2/\Delta i^2} e^{-m{v_i}^2/2k_BT} \tag{4.1}$$

where k_B is Boltzmann's constant, m is the atomic mass and T is the temperature. The distribution describes the interaction volume as Gaussian in 3D. If we project the distribution along the z dimension, the distribution is

$$f(z,t) \propto e^{-mz^2 4ln2/\Delta z^2} \tag{4.2}$$

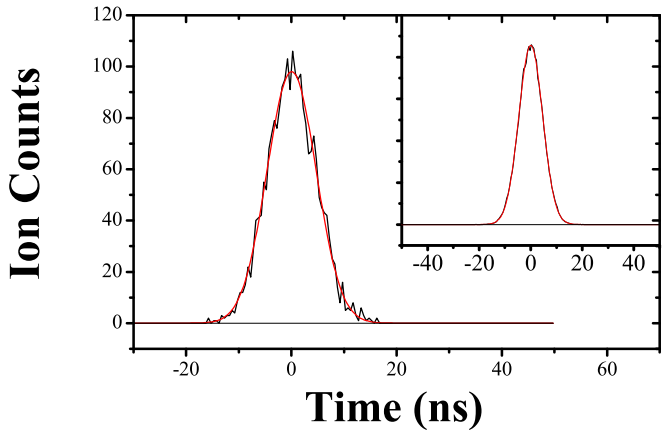

Figure 4.2: Simulated time-of-flight distribution. The major plot is for 3000 counts where the inset is for 100,000 counts.

where Δz is the FWHM of the distribution. The z dimension defines the time-of-flight axis. This is recognized to be a Gaussian distribution of width

$$\Delta z = \sqrt{{\Delta z_0}^2 + \frac{8ln2k_BT}{m}\tau^2} \tag{4.3}$$

where Δz_0 is the FWHM of the excitation volume at $\tau = 0\,\mathrm{s}$. This equation was used to fit the expansion of the cloud as a function of delay to deduce the temperature of the trapped atoms.

Monte Carlo simulations were generated for comparison to the experimental data. The simulations use the temperature and initial Rydberg-atom spatial distribution as input parameters. Figure 4.2 shows a Monte Carlo simulation of a TOF distribution with the same expansion time and number of counts as Fig. 4.3. The inset is the same simulation with 100 000 counts. The simulation matches the experimental data to a high degree of accuracy. The FWHM of the distribution in Fig. 5 is $11.01 \pm 0.04\,\mathrm{ns}$. The experimental data show a Rydberg cloud size of $109.0 \pm 0.5\,\mu\mathrm{m}$ at $\tau = 220\,\mu\mathrm{s}$ and the simulation gives a cloud size of $108.2\,\mu\mathrm{m} \pm 0.4\,\mu\mathrm{m}$. Excellent agreement with the Monte Carlo simulations gives us confidence that all sources of broadening have been minimized and the remaining error is predominantly statistical.

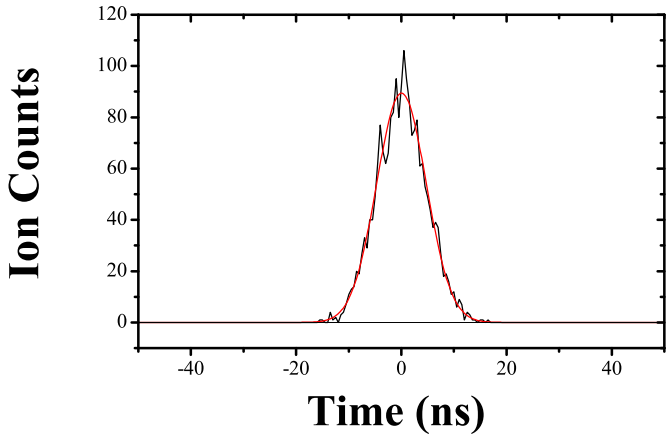

Figure 4.3: Experimental time-of-flight distribution with 3000 counts.

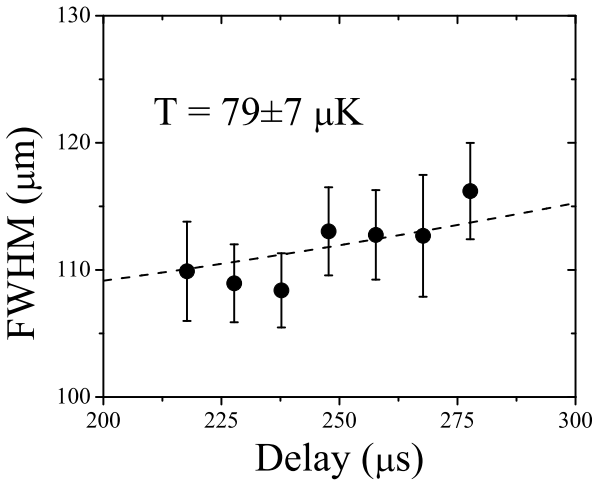

Figure 4.4: Example of a temperature measurement with trapping laser parameters $I = 4\,\mathrm{mW/cm^2}$ in a single trapping beam with $\delta = 2\Gamma$. The temperature is $79 \pm 7\,\mu\mathrm{K}$.

The inset of Fig. 4.2 shows the Monte Carlo simulation obtained with the same parameters but with 100,000 counts. The cloud size for this simulation is $107.9 \pm 0.1\,\mu$m. Accumulating more points gives the predicted $\sqrt{n}$ improvement in error, but the cloud size that was fitted did not change appreciably.

A sample temperature measurement can be seen in fig. 4.4. The dashed line is a fit with eqn. 4.3. The TOF axis has been calibrated to a spatial dimension for the PFI parameters used in this experiment. The initial width of the distribution fits to $105 \pm 7\,\mu$m, which is consistent with our prior measurements of the focal spot size

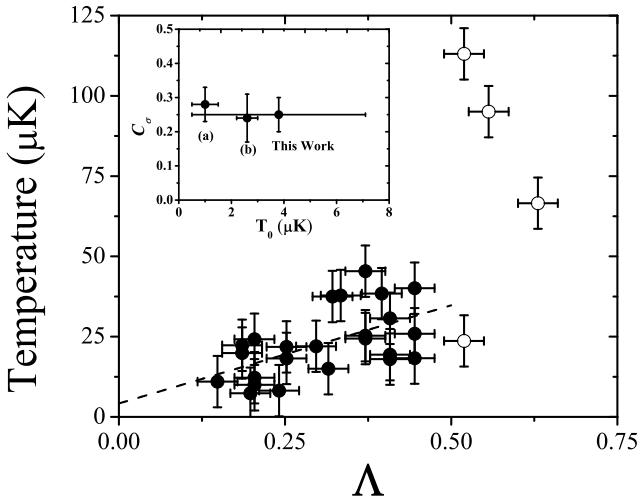

Figure 4.5: Linear fit to the temperature as a function of the light shift parameter, Λ. The inset shows the measured value of C_σ from this work compared to that of other experiments ((a)-[25],(b)-[34]).

on a calibrated CCD and Monte Carlo simulations of the thermal expansion. The temperature is measured to be $79 \pm 7\,\mu$K with trapping parameters of $I = 4\,\mathrm{mW/cm^2}$ in a single trapping beam with $\delta = 2\Gamma$.

The real test of the technique is if the dependence of the temperature on trapping laser parameters follows the dependence of eqn. 3.4 and the measured value of C_σ agrees with the measurements of other experiments [25, 34]. Subdoppler cooling that occurs due to polarization gradients in the cooling beams will cause the measured temperature to be below the Doppler limit of $125\,\mu$K for Cs. Fig. 4.5 shows the dependence of the temperature on the light shift parameter $\Lambda = \Omega^2/|\delta|\Gamma$. For $\Lambda > .5$, the MOT enters the multiple scattering regime and the gas begins to be heated by its own internal light pressure. Fig. 4.5 shows how the measured value of C_σ and T_0 compares to other work and shows that the Rydberg tagging technique is effective for measuring temperatures in the subdoppler regime. The error in T_0 is much larger for our measurements because we are unable to efficiently study the regime of low Λ. In this regime, the MOT density is too low to efficiently accumulate TOF distributions using a steady-state MOT.

There are two important consequences of the measurement. One consequence is that the measurement was done without switching off the magnetic field for the MOT. It was unclear before the experiment was conducted as to whether the magnetic field produced heating of the gas which would cause us to have slightly higher measurements of temperature. Its presence has no measurable effect within the resolution of our experiment. The other consequence is that the uncertainty in the temperature measurements demonstrates the velocity resolution of the spectrometer. The uncertainty for a given temperature measurement was $\pm 7\,\mu$K. This translates to a velocity uncertainty of $\pm 2.5\,$cm/s. This demonstrates the highest resolution ever achieved by Rydberg tagging TOF spectroscopy. Typical velocities of collisions in ultracold collisions are $> 1\,$m/s which would be easily resolvable with our apparatus.

As a result of the temperature measurement, the resolution of the spectrometer has been established. With such a small velocity uncertainty, velocities $> 5\,$cm/s can be resolved. This level of precision is more than adequate to observe the signatures of photo-initiated collision processes or macrodimers with this apparatus.

Chapter 5

Photo-Initiated Collisions

This chapter is devoted to the study of resonant collision processes that occur in Rydberg gases. Excitation at stationary points that arise from avoided crossings between Rydberg atom pair potentials can lead to velocity in excess of the thermal velocity of the atoms in the trap. By monitoring the expansion of the excitation volume while exciting a pair process, extra velocity due to the exit channel of a collision process can be measured.

Fig. 5.1 (a) shows a spectrum taken for the $89D$ state. The spectral feature that this experiment explains is shown to the red of the atomic state. Features such as these do not correspond to an atomic Rydberg state and have been hypothesized to be molecular resonances due to pairs of Rydberg atoms [6]. It is the purpose of these experiments to show that resonances such as these are due to either photo-initiated collision pairs or long range Rydberg atom-Rydberg atom molecules.

The spectrum is overlaid with calculations of dipole interactions of Cs atom pairs [12]. It can be seen that the spectral feature is at the same energy as an avoided crossing. The question this experiment sought to answer, was whether the pair interactions resulted in a bound Rydberg atom-Rydberg atom pair, a macrodimer, or dissociated into a pair of Rydberg atoms with a collision velocity determined by the energy of the exit channel, v_{coll}. By observing the expansion of the TOF distributions with delay τ, the distinction can be made.

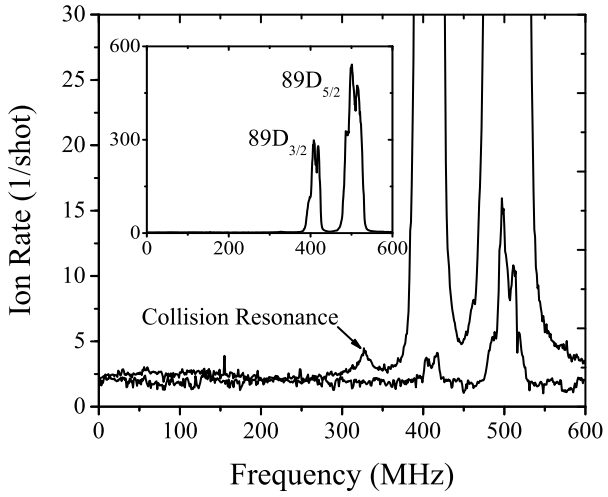

Figure 5.1: Spectra of the 89D state of Cs. The feature to the red of the atomic resonance is a pair process as determined by measurments of the excitation rate dependence at low laser intensity.

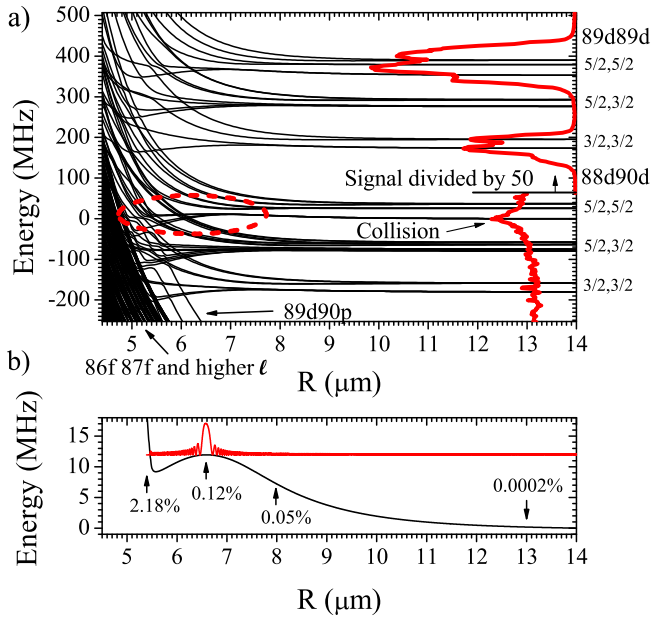

Figure 5.2: (a) Calculated pair potentials in black near the 89D state of Cs. An experimental spectrum is displayed along the right in red with the scale enlarged to show the feature at lower energy. Panel (b) shows and enlargement of the potentials for the region circled in panel (a).

In order to distinguish a pair process as either a photo-initiated collision or a macrodimer, it is sufficient to observe the expansion of the time-of-flight distribution as a function of delay, τ. Fig. 5.3 shows a diagram of the expected width dependence on τ. The atomic state will have a width that is represented by the black line. The expansion of atoms in the absence of collision will be determined by expansion at their thermal velocity. Excitation of a collision process or macrodimer will result in the excitation of two atoms. If two atoms are created at some initial R, the ion pair will Coulomb repel one another after PFI during the time-of-flight. The shorter the initial R, the broader the initial width of the TOF distribution at $\tau = 0$. If the process is a collision, the atoms will recede along R during τ until PFI, and will then be ionized at increasingly larger distances. The Coulomb repulsion for a collision will have less an effect at large τ, until the expansion due to the collision recoil velocity dominates the expansion. This analysis is true for collision velocities as low as a quarter of the Doppler velocity where this technique would not resolve the expansion. However, since the colliding atoms could be prepared at the Doppler velocity to begin with, the dependence would easily be resolved.

A macrodimer will have a different width dependence with increasing τ. Since the molecule would be bound, the distribution of R remains fixed about an average value for narrow linewidth, continuous-wave excitation. As τ increases, the macrodimers will expand at their center of mass thermal velocity, but the extra width due to Coulomb repulsion will remain a constant. In order to observe wavepacket motion in the well, the excitation time would have to be short compared the the classical vibrational period. For the typical well described here, the vibrational period would be of order 1 μs. In order to observe oscillations of the wavepacket, this would require an excitation pulse < 10 ns. To achieve a short pulse with enough energy to have a significant probability to excite a macrodimer, the frequency bandwidth for excitation would be broadened and excite over an energy range larger than the depth of the well.

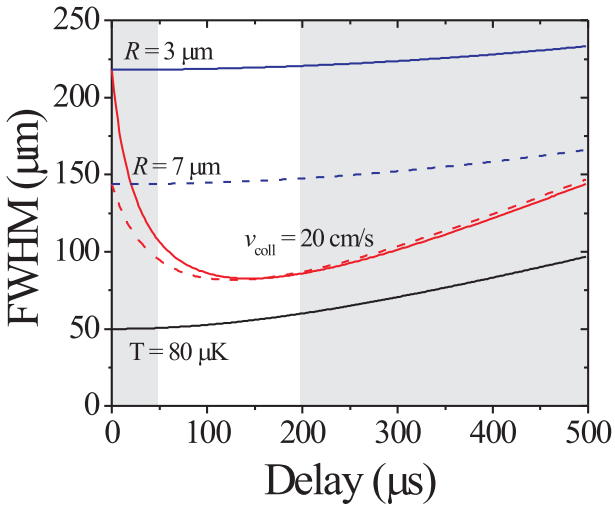

Figure 5.3: Comparison of the time-of-flight distribution for a 20 cm/s photo-initiated collision or a macrodimer. The solid blue line is the width due to a macrodimer created at 3 μm and the solid red line is the width dependence for a collision originating from the same R. Increasing R from 3 to 7 μm yields the dashed curves. The solid black line is the expansion due to temperature alone. All assume an initial excitation volume with a focal spot size of 50 μm. The left gray region is ideal for observing macrodimers while the right region allows measurement of v_{coll}.

This would give a non-negligible contribution to the width from nearby states and obscure the results.

The two delay domains for observing a specific process are shaded in fig. 5.3. The shaded region to the left is the region where it would be advantageous to observe molecules. For τ short compared to the atomic lifetime, a Coulomb broadened signal should be clearly visible that does not decrease with increasing τ. To observe the velocity due to a photo-initiated collision, long times are desirable (right shaded region). The asymptotic expansion will be due to the collision recoil velocity and will not be obscured by Coulomb repulsion. The long lifetimes of Rydberg states permits the measurement of small collision velocities, because a significant fraction of excited atoms exist for hundreds of microseconds at large n.

The Rydberg atoms are excited using a two-photon scheme. The light for the first step is generated by a tunable dye laser (Coherent 599-21), A, which is resonant with $6S_{1/2}(F{=}4) \rightarrow 6P_{3/2}(F{=}5)$ at $\lambda_A \sim 852$ nm. The laser is collimated to the size of the

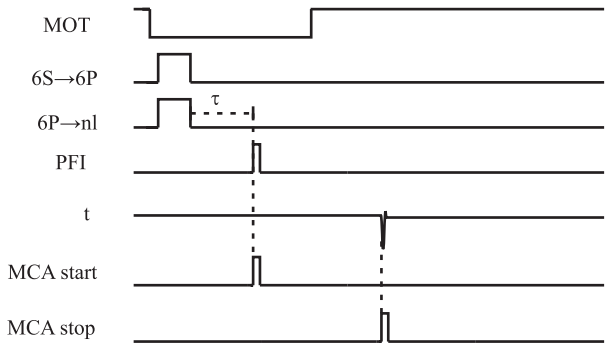

Figure 5.4: Timing diagram for the measurements of the 88D+90D pair resonance.

MOT, ($\sim 1\,$mm), and the intensity was fixed at $I_A = 4\,\mathrm{mW/cm^2}$. The linewidth of A is $\sim 2\,$MHz.

A second frequency stabilized dye laser (Coherent 699-21), B, at $\lambda_B \sim 508\,$nm excites atoms to states in the energy region near n$\sim$ 89 from $6P_{3/2}(F = 5)$. Laser B is transported to the MOT through a single mode optical fiber to spatially filter the light. The peak power at the end of the fiber is $\sim 17\,$mW. The beam waist of laser B at the MOT is $104 \pm 7\,\mu$m, as confirmed by imaging the focal spot on a CCD. The frequency of laser B is referenced to a wavemeter with 80 MHz resolution and an I_2 cell to an absolute accuracy of 2 MHz.

The timing diagram can be seen in fig. 5.4. Before Rydberg excitation, the trapping light is extinguished for $2.5\,\mu$s and remains off until after the detection phase of the experiments. After the trap is shut off, the excitation lasers are pulsed on using acousto-optic modulators to excite the Rydberg atoms. Laser A is gated on with a pulse width of $2.5\,\mu$s. Laser B is gated on for $1\,\mu$s so that both lasers overlap in time. The laser power is monitored using a photodiode. There are $\sim 10^5$ atoms in the laser-MOT interaction region available for excitation.

Pulsed-field ionization is used to measure the production of Rydberg atoms. A $4\,\mu$s high voltage pulse with an amplitude of $320\,V$ (field $E = 53\,\mathrm{V/cm}$) is applied across the extraction plates to field ionize the Rydberg atoms and accelerate the resulting ions to the MCP.

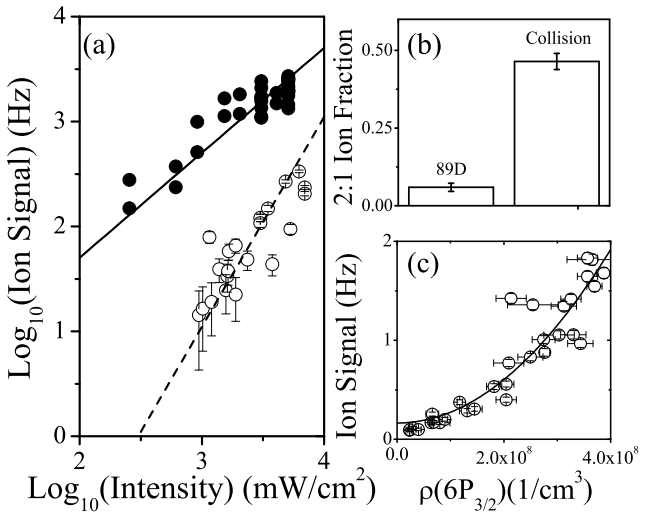

Figure 5.5: (a) Excitation rate on a log-log plot as a function of I_B. Panel (b) shows the charge distribution on the atomic line and pair resonance at low count rates ($\sim 10\,\mathrm{Hz}$). Panel (c) shows that with I_B fixed and varying I_A that the excitation rate is also quadratic.

Identification of the collision process was accomplished by three separate measurements. We measured the rate of collision events as a function of I_B to determine the number of photons involved. We verified that the spectral feature is a binary atomic process by analyzing the charge distribution of the ions detected during each event. Finally, we measured the velocity of the fragments leaving the collision to identify the exit channel.

The signal rate from the $89D_{3/2}$ atomic resonance and collision resonance were measured simultaneously by scanning laser B in 1 MHz steps. I_A was fixed during the experiment to provide a constant initial $6P_{3/2}(F = 5)$ density. To minimize loss of signal due to Rydberg decay and avoid cold plasma effects, the delay between excitation and pulsed field ionization was $1\,\mu$s. The atoms move $\sim 70\,$nm in this time at our temperature. The spectral lines that were measured were fit to Lorentzian line profiles. Fig. 5.5 shows the ion yield at the peak of the collision resonance and atomic resonance as a function of I_B.

The ion production rate for a single photon event at low intensity, W_1, scales

linearly with I_B. $W_1 = \sigma^{(1)}(\nu)I_B$, where $\sigma(\nu)$ is the single photon cross-section for excitation at frequency ν. The ion production rate for a two-photon event, W_2, scales as I_B^2. $W_2 = \sigma^{(2)}(\nu)I_B^2$, where $\sigma^{(2)}(\nu)$ is the two photon cross-section for excitation at frequency ν. Consequently, a single photon event will have a slope of 1 and a two photon process will have a slope of 2 on a log-log plot of rate vs. intensity, fig. 5.5. The data shown in fig. 5.5 clearly indicates that the collision resonance is excited via a two photon process.

To confirm that the spectral feature corresponding to the collision is the result of a 2 atom process, we analyzed the pulse height distribution of the charge accumulated during each cycle of the experiment at low laser B intensity. The charge produced on the MCP after each event is proportional to the number of particles that hit. At low laser B intensity, where much less than 1 event occurs per laser shot, the pulse height distribution of the amplified charge indicates the average number of particles that are produced during each event.

The probability of exciting N_{Ryd} Rydberg atoms is determined by the binomial distribution

$$P(N_{Ryd}) = \frac{N_{atoms}!}{N_{Ryd}!(N_{atoms} - N_{Ryd})!} {p_{exc}}^{N_{Ryd}} (1 - p_{exc})^{N_{atoms} - N_{Ryd}} \tag{5.1}$$

where p_{exc} is the probability of exciting $N_{Ryd} = 1$ atom for a single photon excitation, or $N_{Ryd} = 2$ for a two-photon excitation of a pair. N_{atoms} is the number of available atoms in the $6P$ state. p_{exc} depends on I_B so I_B must be kept small to avoid multiple excitations.

The detection efficiency P_D of Rydberg atoms is determined by decay, the quantum efficiency of the MCP, and transmission through the MCP grid. At short PFI delay, $\tau = 1\,\mu$s, essentially all the Rydberg atoms that are excited survive. The MCP quantum efficiency is $\eta \sim 60\%$ for Cs^+ at 4.5 keV [49], and the grid transmission is $t \sim 86\%$, yielding $P_D \sim \eta \times t = 52\%$

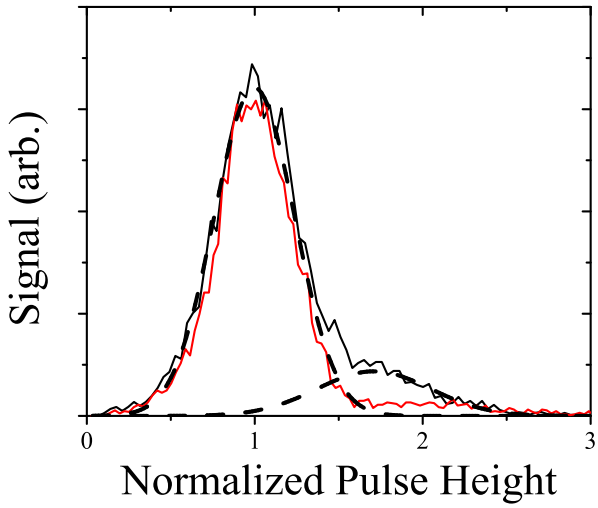

Figure 5.6: Pulse height distributions for the $89D$ state (in red) and the pair resonance (in black). Fits for the pair resonance are shown as dashed Gaussian distributions.

We verified P_D for the experiment by simultaneous measurements of ion yield and trap loss. I_B was frequency scanned across the $89D_{3/2}$ state. The ion yield was measured while a simultaneous trap loss spectra was taken with a calibrated photomultiplier tube. The absorption rate was measured for the range $15\,\mathrm{mW/cm^2} < I_B < 100\,\mathrm{mW/cm^2}$ by monitoring the trap loss rate ${\tau_{trap}}^{-1}$ when $I_B = 0$. The absorption rate is given

$$\gamma(I_B) = \frac{N_{atoms} - {N_{atoms}}'(I_B)}{\tau_{trap}{N_{atoms}}'(I_B)} \tag{5.2}$$

where ${N_{atoms}}'$ is the number of $6P$ atoms with the additional loss due to I_B. By measuring the loading rate of the MOT, $\tau = 6.2 \pm 0.1\,\mathrm{s}$. The ion detection rate R_{ion} for $I_B < 4\,\mathrm{mW/cm^2}$ was compared to the number of atoms that were excited according to $\gamma(I_B)$, and $P_D = R_{ion}/\gamma(I_B) = 0.47 \pm 0.06$ which agrees with the estimate based on the MCP quantum efficiency and grid transmission.

A sample pulse height distribution can be seen in fig. 5.6. A distribution for the $89D$ state is in red and for the pair resonance in black. The black dashed curves are Gaussian fits to the pair resonance distribution. The width of the distribution scales

as $\sqrt{q}$ where q is the charge [49]. An increase in 2 charge detections for the pair resonance is clear from the pulse height distributions as evidenced by the increase in signal at higher pulse height.

Fig. 5.5(b) shows the comparison of the fraction of 2 to 1 ion counts when pulse height distributions were accumulated at the frequency of the $89D$ state and at the frequency of the resonance feature. The measurements were taken at a rate of 1 kHz with an ion rate of ~ 20 Hz. The resonance feature shows an increase in 2 to 1 ion counts that identifies it as a pair process, and gives a measurement of $P_D = 0.46 \pm 0.06$, consistent with expectations.

To further confirm this result, I_A was varied to change the $6P$ density while monitoring R_{ion}. The results are shown in fig. 5.5(c). The quadratic dependence on I_A indicates that two $6P$ atoms are involved in the excitation of the resonance, also identifying it as a pair process.

After establishing that the resonance feature was due to pairs of Rydberg atoms, TOF distributions of the fragments were measured as a function of delay τ to deduce the recoil velocity. At short delay, a constant Coulomb broadened width was not observed, so longer delays were used in the measurements to measure the collision channel recoil velocity, v_{coll}.

The experiment was repeated at a rate of 1 kHz. The charge from each event is monitored and typical count rates are ≤ 100 Hz to prevent coulomb broadening. The range of delays was chosen so that the data could be acquired at the same intensity of I_B ($\sim 10\,\mathrm{mW/cm^2}$). The initial delay of $200\,\mu$s was chosen to have sufficient expansion at the collision velocity relative to the thermal velocity.

The thermal expansion of the trapped Rydberg atoms was measured as a control [28]. We measured the temperature of atoms (solid circles) in the $6S_{1/2}(F = 4)$ state of the MOT to be $79 \pm 7\,\mu$K by tuning laser B to the $89D_{5/2}$ atomic Rydberg resonance.

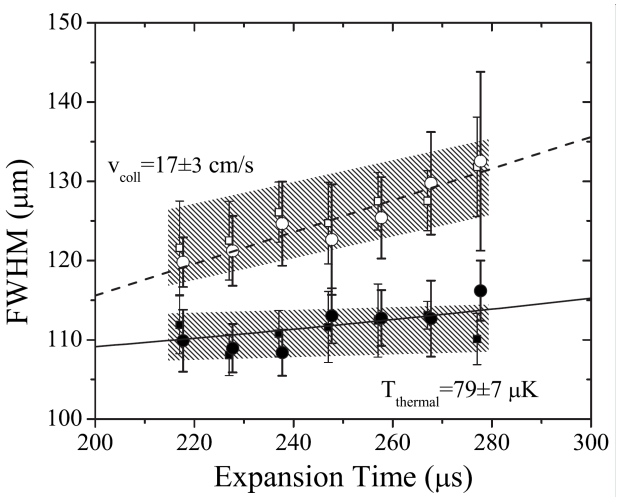

Figure 5.7: Measurement of the recoil velocity of the pair resonance that identifies it as a photo-initiated collision. The collision is shown by the hollow circles and a temperature measurement from the atomic line is shown in the solid circles for comparison. The squares are points simulated by Monte Carlo with similar numbers of ion counts compared to the experiment. The gray regions are confidence bands determined by the simulation.

The data is shown in fig. 5.7. The laser polarization was parallel to the TOF axis for the data shown in fig. 5.7. The experiment was repeated with the polarization perpendicular to the TOF axis and no difference from the parallel configuration was observed. The collision velocity is sufficiently low that the velocity distributions fit well to a Gaussian. The exit channel velocity, v_{coll}, of the atoms after the collision was measured to be $17 \pm 3\,\mathrm{cm/s}$ (empty circles in fig. 5.7).

The collision data was simulated by Monte Carlo methods (empty squares in fig. 5.7) to determine the exit channel velocity [12]. The input parameters for the simulations were the temperature of the MOT and the energy difference between the known, two-photon excitation energy and the asymptotes of pair states in the energy region of $89D$. Calculated pair potentials [12] and a ion yield spectrum are shown in fig. 5.2 (a).

Fig. 5.2 (b) shows the square of the wavefunction as a function of R. The barrier at short R mixes with the nearby $89D$ state by a percentage indicated on the figure.

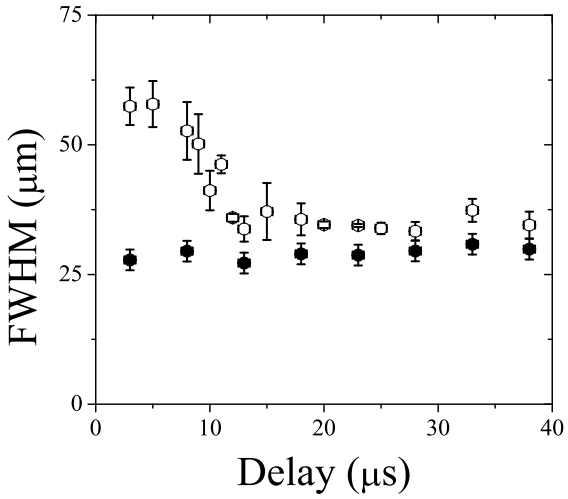

Figure 5.8: TOF distribution dependence for small delay. Empty circles are the data for the $88D_{5/2} + 90D_{5/2}$ resonance feature while the solid circles are for the $89D_{5/2}$ atomic state. The focus of Laser B was $\sim 25\,\mu$m for these measurements to more clearly observe the Coulomb broadening at short delay, τ.

This, together with the stationary point on top of the barrier, enhances the probability of exciting the collision process. The measured exit velocity agrees with the products exiting along the $88D_{5/2}+90D_{5/2}$ asymptote from the barrier which predicts a velocity of $19 \pm 4\,$cm/s. The excellent agreement between the experiment and theory gave us confidence we could identify a pair resonance as a photo-initiated collision or macrodimer by comparison to the calculated pair potentials.

It is also informative to observe the TOF distributions at short delay to verify the dependence of the Coulomb repulsion as the collision fragments recede along R. A short delay measurement can be seen in fig. 5.8. Laser B was focused to $\sim 25\,\mu$m to more clearly observe the effects due to Coulomb repulsion. The distribution is clearly larger for $\tau < 10\,\mu$s as the fragments expand. The non-linearity of the FWHM dependence on τ can be attributed to the acceleration of the particles along the pair potential. Had the $88D_{5/2} + 90D_{5/2}$ resonance feature resulted in a bound molecule, the width would be expected to be constant over the range of delays shown.

The existence of photo-initiated collisions illustrates that additional spectral fea-

tures in Rydberg spectroscopy cannot be attributed to macrodimers outright. It is necessary to conduct further studies to verify the existence of bound states other than by purely spectroscopic methods. With the measurement of the recoil velocity due to a photo-initiated collision, we now have confidence that we can observe the signature of the Coulomb repulsion on the time-of-flight distribution due to macrodimers.

Chapter 6

Observation of Cs Macrodimers

This chapter presents the observation of a new type of molecule that is comprised of two Rydberg atoms bound at long range. Macrodimers are observed by monitoring the Coulomb broadening of the TOF distributions due to the repulsion of the macrodimer ion fragments after PFI. The delay dependence of the TOF width was compared to Monte Carlo simulations of a collision that originated at the same internuclear separation as the observed macrodimer. These measurements show that the observed pair resonances are bound to within the resolution of the spectrometer.

Long range molecules are excited by a two-photon process

$$\begin{aligned} &\mathrm{Cs}[6P_{3/2}(F=5)] + \mathrm{Cs}[6P_{3/2}(F=5)] + 2h\nu \\ &\quad \rightarrow \mathrm{Cs}_2[(n-1)D_{5/2} + (n+1)D_{5/2}]. \end{aligned} \tag{6.1}$$

The atoms in the $6P_{3/2}(F=5)$ state are excited from the $6S_{1/2}(F=4)$ state using a beam derived from the trapping laser with a FWHM$\sim 2\,$mm. This beam is crossed with a dye laser used to excite to high principal quantum number ($n \sim 65$) Rydberg states ($\lambda = 508 - 509\,$nm). The dye laser is focused to FWHM$\sim 25\,\mu$m and the polarization is parallel to the time-of-flight (TOF) axis. The crossed geometry helps reduce background counts.

One of the molecular resonances under study is shown in fig. 6.1. It is plotted in

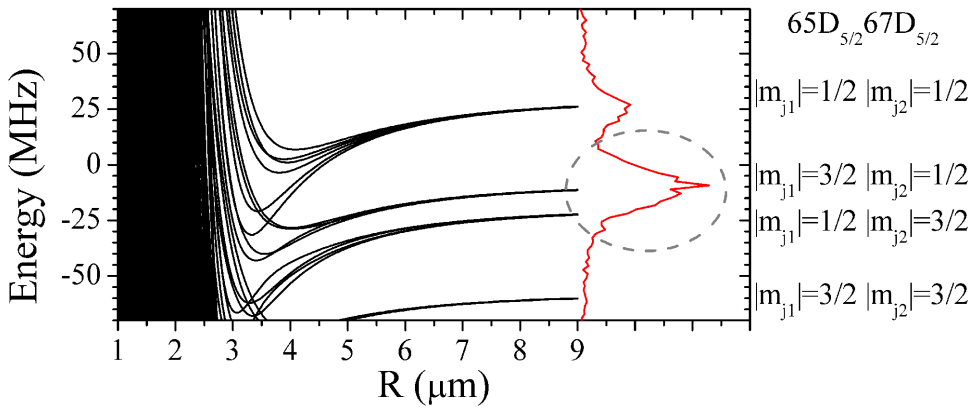

Figure 6.1: Integrated atomic ion yield spectra and pair potentials for $65D+67D$ with $\epsilon = 190\,\mathrm{mV/cm}$. The excitation laser intensity is $\sim 500\,\mathrm{W/cm^2}$. All Fine structure and Ω are plotted. $\Omega = m_{j1} + m_{j2}$ is the projection of the angular momentum on R. The feature in the figure studied for this pair of states is circled.

red along the calculations of the pair interaction potentials described in [13]. Prominent wells are shown in the calculations that gave us confidence that the observed resonance feature should result in a bound macrodimer. The depth of the well and the strength of the feature were good indications that the characteristic TOF signature could be observed.

The timing of the experiment is as follows (see fig. 6.2). The $6S_{1/2}(F = 4) \rightarrow 6P_{3/2}(F = 5)$ trapping light is switched off with an acousto-optic (AO) for $10\,\mu$s. $2.5\,\mu$s after this light is off, the Rydberg excitation beams are switched on with AOs for $5\,\mu$s. After a variable delay, τ, PFI is applied for $2\,\mu$s at $66\,\mathrm{V/cm}$. A $1\,\mathrm{V}/\mu$s, $5\,\mu$s duration ramp is applied immediately preceding the PFI pulse to clear any stray ions from the excitation region. The ionized atoms/molecules have a TOF of $25\,\mu$s after PFI before detection on the MCP. The timing signals from the MCP are processed by a constant fraction discriminator and accumulated by a multichannel analyzer (MCA). The falling edge of the PFI is used to trigger acquisition for the MCA. The $6S_{1/2}(F = 3) \rightarrow 6P_{3/2}(F = 4)$ repumping light for the MOT is on during the entire experiment. A constant voltage is applied to the upper field plate during excitation. The applied electric field is interrupted only during PFI. The experiment was repeated

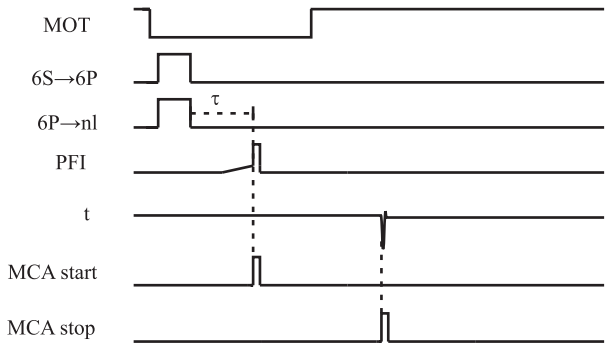

Figure 6.2: Timing diagram for the macrodimer TOF measurements. The timing is similar to the timing for the photo-initiated collision measurement, with the addition of a short ramp prior to PFI. This ramp helps remove any stray ions from the excitation volume.

at a rate of 1 kHz.

Molecular resonances are observed for Rydberg atom pairs at different applied electric field. We measured molecular resonances for the $63D$+$65D$, $64D$+$66D$, $65D$+$67D$ and $66D + 68D$ states. The excitation rate for each molecular resonance was measured as a function of intensity (see fig. 6.4(b)). The rates depend quadratically on the intensity which indicates that the resonances are two-photon transitions from the initial $6P_{3/2}$ state.

The potential wells probed with our experiment depend strongly on the applied electric field. Sample spectra for molecular resonances in the $65D + 67D$ manifold can be seen in fig. 6.3. Panel (a) shows the spectrum with the applied field used to measure the Coulomb repulsion of the fragments. Panel (b) shows the same spectral region at slightly higher field where the resonances have disappeared. At zero field, calculations of the region do not display any of the prominent wells shown in fig. 6.1. As the field is increased, the Stark fans due to the higher angular momentum states are pushed to lower energy, forming avoided crossings that support bound states. As the field is increased further, the higher fan states begin interacting more strongly and the wells are destabilized.

We compared the shape of the TOF distribution for single thermal atoms to

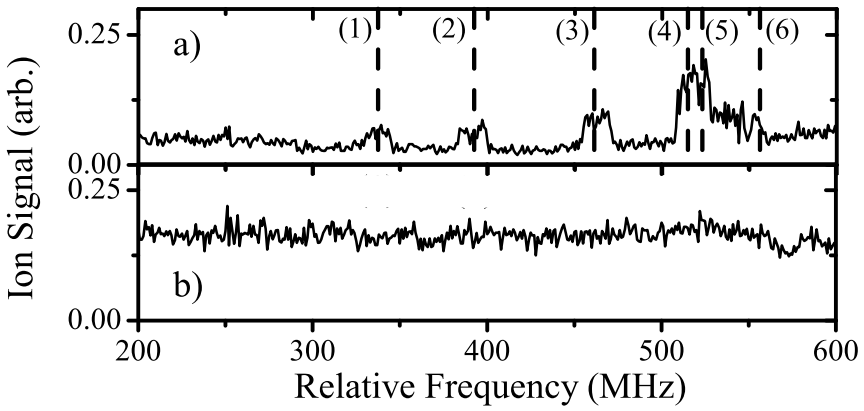

Figure 6.3: Spectra near the $66D$ state taken for an applied field of (a) 190 mV/cm and (b) 264 mV/cm. The modest increase in electric field is sufficient to destroy the pair resonance. The m_j for the $65D_{5/2}$+$67D_{5/2}$ states are (1)-(1/2,5/2), (2)-(5/2,1/2), (3)-(3/2,3/2), (4)-(1/2,3/2), (5)-(3/2,1/2), and (6)-(1/2,1/2).

bound pairs including Coulomb repulsion after PFI (see fig. 6.4(a)). The molecular signal is much broader than the atomic signal, characteristic of the Coulomb repulsion between the ions. The molecular signal appears to exhibit maxima symmetric about the peak center, suggestive of an alignment effect between the TOF axis, transition dipole moment, and dye laser polarization [50]. We measured the TOF distribution for the molecular resonance with the dye laser polarization perpendicular to the TOF axis and observed no difference in the observed width or shape. If alignment of the molecule is present, it could be due to the applied electric field. We currently have no experimental way of verifying this without major modifications to the experiment which could adversely affect the resolution of our spectrometer.

TOF distributions were accumulated for $\tau = 18 - 38\,\mu$s (see fig. 6.5). The times were chosen to be short enough to avoid decay of one of the molecular partners, but long enough to measure the width dependence on τ. The lifetime of a $\sim 60D$ state including blackbody decay is $\sim 100\,\mu$s so delays $< 50\,\mu$s should minimize the probability of decay by one of the partners [19, 20]. For our spectrometer geometry, applied field, and PFI, 11 ns corresponds to a spatial width of 25 μm. The atomic

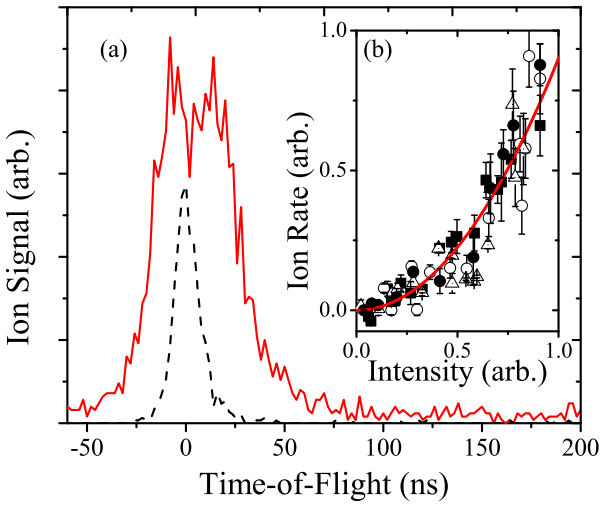

Figure 6.4: Panel (a) shows the time-of-flight distribution for the $65D$+$67D$ molecular state at a delay of $38\,\mu$s in red compared to the $66D$ atomic state in black. The molecular resonance shows pronounced Coulomb broadening. Panel (b) shows the excitation rate as a function of dye laser intensity, indicating that the process is two-photon.

measurement is large by $\sim 50\,\%$, most likely due to alignment difficulties of the dye laser focal spot, but presents no difficulties for observing the Coulomb repulsion which is a factor of at least 3 larger in width.

The width was simulated using Monte Carlo. A range in R was chosen for input based on the calculated potential wells. The simulated width was in good agreement with the molecular TOF signal. The Monte Carlo included the field due to the PFI and applied field during the entire TOF. The Monte Carlo simulation was consistent with the TOF measured by the experiment as well as the distribution width at the MCP.

We compared the measured molecular TOF distributions to simulations of collision velocity to determine that the molecules were bound until PFI. We do not expect to observe oscillations of the TOF width because the entire well will be populated as the vibrational period ($\tau_{vib} < 2\,\mu$s) is less than the excitation time and much less than τ. The width dependence on delay was compared to the same R at $\tau = 0$ with the addition of thermal velocity. This gives us confidence that we can distinguish between

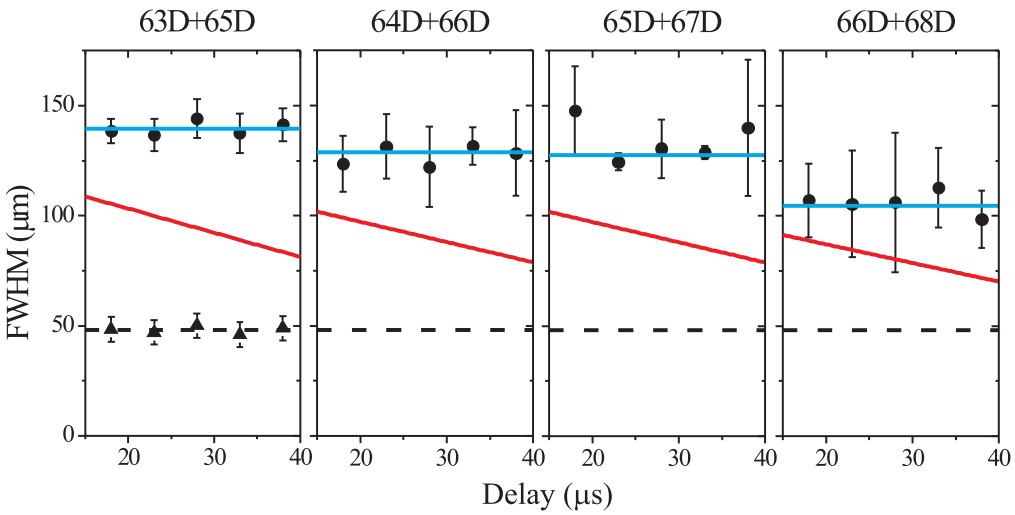

Figure 6.5: Coulomb broadened width for the $63D + 65D$, $64D + 66D$, $65D + 67D$, and $66D + 68D$ molecular states shown with solid circles with a constant fit in blue. The red is a Monte Carlo simulation of the expected behavior if the molecular resonance was due to a photo-initiated collision with recoil velocity equal to the Doppler velocity. The triangles are a measurement of temperature taken for the $66D$ state for comparison fit with a dashed line.

a bound molecule and a low velocity photo-initiated collision as observed previously [14]. The simulated width decreases rapidly even for thermal velocity.

A linear fit was applied to each molecular pair expansion to determine the minimum collision velocity that would give similar results. The velocity allowed by the error in the molecular TOF signal is $0 \pm 1\,\mathrm{cm/s}$ for $63D + 65D$, $-2.7 \pm 2.1\,\mathrm{cm/s}$ for $64D + 66D$, $2.2 \pm 2.7\,\mathrm{cm/s}$ for $65D + 67D$ and $3.4 \pm 4\,\mathrm{cm/s}$ for $66D + 68D$. The electric fields that were applied during the measurements were $\epsilon = 224\,\mathrm{mV/cm}$, $\epsilon = 205\,\mathrm{mV/cm}$, $\epsilon = 190\,\mathrm{mV/cm}$, and $\epsilon = 158\,\mathrm{mV/cm}$ respectively. The width is constant to within the resolution of our spectrometer for all pairs with the exception of the $66D + 68D$ pair [14, 28]. The $66D + 68D$ pair is still in agreement with a fit to a constant value. The highest pair state is the only state that would be in agreement with a pair of free atoms moving relative to each other with the velocity determined by an $80\,\mu\mathrm{K}$ gas ($7.1\,\mathrm{cm/s}$). The lower three pairs would represent unphysically cold atoms for the experiment and would be more reasonably interpreted as bound. Even

for the lowest pair state, if they could be explained as free atoms pairs moving with thermal velocity, there must still be a mechanism for excitation at an initial R that contributes Coulomb repulsion.

The range of n used in our experiment is limited by the proximity to the nearest atomic line. The proximity to the line has two consequences. First, the excitation rate decreases for lower n. This is because most of the excitation probability is due to mixing with the nearest atomic state by an off-resonant two-photon transition from an initial pair of $6P_{3/2}$ atoms. The second consequence is that the signal becomes obscured for higher n as the molecular resonance moves into the wing of the atomic line. This can be seen in the measurements. As n increases, the TOF distributions contain more noise and decrease in width. As the range of R for these states does not vary much with n, the marked decrease in width and increase in noise is at least partly attributed to additional signal from the atomic line.

These measurements show that macrodimers exist for a range of n consistent with calculated pair interaction potentials due to multipolar interactions. The dependence of the wells on the applied electric field has been shown to be important in any experiment where robust creation of macrodimers is desired.

Chapter 7

Conclusions and Future Directions

The most significant contribution of this work is the ability to experimentally distinguish between a photo-initiated collision and the creation of a macrodimer in an ultracold system with the application of an electric field. This experimental work suggests the calculations performed in [12, 13] accurately describe the dominant interactions. Together with the ability to calculate the pair interaction potentials to high precision, macrodimers can be produced in the lab for future studies of weak interactions [2, 13]. Macrodimers should also be observable in other ultracold alkali samples. With robust production of macrodimers, experiments could be conducted that study the electric field dependence of the multipole interactions as well as other sensitive tests of theory. The techniques described could also be applied to study ionizing collisions in Rydberg gases that leads to the formation of ultracold plasmas [51].

The measurement of small recoil velocities due to collisions between Rydberg atoms and Coulomb repulsion between pairs, opens up a new avenue of ultracold research. The apparatus described in this work can be extended to more complex studies of ultracold collisions and ultracold chemistry. The future of this experiment lies in experiments involving ultracold atom-diatom collisions. The 3D angular

distribution of the products in the collision

$$Cs + Cs + Cs \rightarrow Cs_2 + Cs \tag{7.1}$$

will be determined by the 3-body potential. This apparatus could be used for sensitive tests of 3-body recombination theory. The unprecedented resolution of this apparatus makes it possible to resolve the velocity signature of virtually all collision processes that occur at ultracold temperatures.

Of immediate interest would be to investigate the angular dependence on the creation of the macrodimers. By performing measurements of the angular distribution of the products in 3D, it should be possible to determine if the applied electric field in these experiments provides a spatial alignment effect that cannot be observed in the current experiments. With the addition of a dipole trap for increased atomic density, measurements of the 3D angular distribution should be feasible by increasing the number of available pairs at the necessary internuclear separation. Studying the anisotropy of the multipolar interactions could have implications on the future of using Rydberg atoms for quantum information processing. It may be that there are preferred orientations of the interacting atomic pairs that would lead to longer coherence times. Experiments that rely on ordering atoms in microtraps might significantly benefit from studies of this kind. With this apparatus, it is possible to study the 3-D interactions of ultracold atoms in an anisotropic potential.

Another avenue of future research could be to study the state distribution of the macrodimers as a function of delay. From the work done previously with resonant energy transfer, it might be expected that energy could be exchanged between the atoms that constitute the macrodimer [1]. By studying the long term dependence of the time-of-flight width versus delay, together with state selective ionization, the lifetime of the macrodimers produced in these experiments could be studied further.

It is clear that much can be accomplished using the techniques described in this

work to study ultracold collision dynamics. The techniques described are not restricted to studies of Rydberg interactions, but are instead widely applicable to other systems. Such multi-differential techniques can yield a wealth of information about collision dynamics in ultracold systems.

7.1 Publications

The following publications resulted directly from this work:

- K. Overstreet, J. Franklin and J.P. Shaffer, "Zeeman effect spectroscopically locked Cs diode laser for atomic physics" Rev. Sci. Instrum. **75**, 4749 (2004).
- Arne Schwettmann, Jack Franklin, K. Richard Overstreet, and James P. Shaffer, "Stark slowing asymmetric rotors: Weak-field-seeking states and nonadiabatic transitions" J. Chem. Phys. **123**, 194305 (2005).
- K. R. Overstreet, P. Zabawa, J. Tallant, A. Schwettmann, and J. P. Shaffer, "Multiple scattering and the density distribution of a Cs MOT" Opt. Express **13**, 9672 (2005).
- J. Tallant, K. R. Overstreet, A. Schwettmann, and J. P. Shaffer , "Sub-Doppler magneto-optical trap temperatures measured using Rydberg tagging" Phys. Rev. A **74**, 023410 (2006).
- Arne Schwettmann, Jeff Crawford, K. Richard Overstreet, and James P. Shaffer, "Cold Cs Rydberg-gas interactions" Phys. Rev. A **74**, 020701 (2006).
- K. Richard Overstreet, Arne Schwettmann, Jonathan Tallant, and James P. Shaffer, "Photoinitiated collisions between cold Cs Rydberg atoms" Phys. Rev. A **76**, 011403 (2007).

- Arne Schwettmann, Chris McGuffey, Savith Chauhan, K. Richard Overstreet, and James P. Shaffer, "Tunable four-pass narrow spectral bandwidth amplifier for use at $\sim 508\,\mathrm{nm}$" Appl. Opt. **46**, 1310 (2007).

- Arne Schwettmann, K. Richard Overstreet, Jonathan Tallant, and James P. Shaffer, "Analysis of long-range Cs Rydberg potential wells" J. Mod. Opt. **54**, 2551 (2007).

- K. R. Overstreet, A. Schwettmann, J. Tallant, D. Booth, and J. P. Shaffer, "Observation of Cs Rydberg atom macrodimers" (*in submission*).

7.2 Presentations

This work has been presented on many occasions at conferences and universities. The following is the list of presentations that resulted from this work:

- K. Overstreet, B. Chung, J. Crawford, J. Tallant and J. P. Shaffer, "Photofragment Imaging of Ultracold Collisions" DAMOP, Tucson, AZ, (2004).

- K. Overstreet, J. Tallant, J. Crawford, B. Chung and James P. Shaffer, "Cold Rydberg Gas Collisions" OSA/LS, Rochester, NY, (2004).(*Invited*)

- K. Richard Overstreet, Jonathan Tallant, Jeff Crawford, Arne Schwettmann, and James P. Shaffer, "Cold Cs Rydberg Atom Collisions: Line Shifts, Broadening and Inelastic Processes" DAMOP, Lincoln, NE, (2005).

- K. Richard Overstreet, Jonathan Tallant, Jeff Crawford, Arne Schwettmann, and James P. Shaffer, "Rydberg Atom Interaction in Cold Cesium" Institute for Atomic and Molecular Physics, Harvard Smithsonian Institute for Astrophysics, Cambridge, MA, (2005). (*Invited*)

- K. Richard Overstreet, Jonathan Tallant, Arne Schwettmann, Jeff Crawford, and James P. Shaffer, "Long Range Interactions and Collisions in a Cold Cs Rydberg Gas" OSA/LS, Tuscon, AZ, (2005).

- Arne Schwettmann, Jeff Crawford, K. Richard Overstreet, and James P. Shaffer, "Rydberg Atom - Rydberg Atom Dipole-Dipole Potentials" DAMOP, Knoxville, TN (2006).

- Arne Schwettmann, Jack Franklin, K. Richard Overstreet, Jonathan Tallant, and James P. Shaffer, "Stark Slowing of Asymmetric Rotors" DAMOP, Knoxville, TN (2006).

- Jonathan Tallant , K. Richard Overstreet , Arne Schwettmann , Jeff Crawford , and James P. Shaffer, "Temperature measurements using Rydberg tagging" DAMOP, Knoxville, TN (2006).

- K. Richard Overstreet, Patrick Zabawa, Jonathan Tallant, Arne Schwettmann, Jeff Crawford, and James P. Shaffer, "Abel inversion for study of multiple scattering in a Cs magneto-optical trap" DAMOP, Knoxville, TN (2006).

- K. Richard Overstreet, Arne Schwettmann, Jonathan Tallant, and James P. Shaffer, "Resonant collision processes in a Cs Rydberg gas" DAMOP, Calgary, Alberta, Canada (2007).

- Arne Schwettmann, K. Richard Overstreet, Jonathan Tallant, and James P. Shaffer "Long-range Cs Rydberg molecules" DAMOP, Calgary, Alberta, Canada (2007).

- Jonathan Tallant, K. Richard Overstreet, Arne Schwettmann, and James P. Shaffer, "Rydberg tagging time-of-flight imaging to study ultracold collisions" DAMOP, Calgary, Alberta, Canada (2007).

- K. Richard Overstreet, Arne Schwettmann, Jonathan Tallant and James P. Shaffer, "Long Range, Cold Cs Rydberg Atom-Rydberg Atom Molecules" DAMOP, State College, PA (2008).

- Jonathan Tallant, K. Richard Overstreet, Arne Schwettmann, and James P. Shaffer, "Dipole-Dipole Interactions in a Cold Cs Rydberg Gas" DAMOP, State College, PA (2008).

Bibliography

[1] T. F. Gallagher, K. A. Safinya, F. Gounand, J. F. Delpech, W. Sandner, and R. Kachru, Phys. Rev. A. **25**, 1905 (1982).

[2] C. Boisseau,I. Simbotin, and R. Côté, Phys. Rev. Lett. **88**, 133004 (2002).

[3] D. Jaksch, J. I. Cirac, P. Zoller, S. L. Rolston, R. Côté, and M. D. Lukin, Phys. Rev. Lett. **85**, 2208 (2000).

[4] M. D. Lukin, M. Fleischhauer, R. Côté, L.. M. Duan, D. Jaksch, J. I. Cirac, and P. Zoller, Phys. Rev. Lett., **87**, 037901 (2001).

[5] A. L. de Oliveira, M. W. Mancini, V. S. Bagnato, and L. G. Marcassa, Phys. Rev. Lett., **90**, 143002 (2003).

[6] S. M. Farooqi, D. tong, S. Krishnan, J.Stanojevic, Y. P. Zhang, J. R. Ensher, A. S. Estrin, C. Boisseau, R. Côté, E. E. Eyler, and P. L. Gould, Phys. Rev. Lett., **91**, 183002 (2003).

[7] D. Tong, S. M. Farooqi, J. Stanojevic, S. Krishnan, Y. P. Zhang, R. Côté, E. E. Eyler, and P. L. Gould, Phys. Rev. Lett., **93**, 063001 (2004).

[8] K. Singer, M. Reetz-Lamour, T. Amthor, L. G. Marcassa, and M. Weidemuller, Phys. Rev. Lett., **93**, 163001 (2004).

[9] T. C. Liebisch, A. Reinhard, P. R. Berman, and G. Raithel, Phys. Rev. Lett., **95**, 253002 (2005).

[10] A. Fioretti, D. Comparat, C. Drag, T. F. Gallagher, and P. Pillet, Phys. Rev. Lett. **82**, 1839 (1999).

[11] M. R. Flannery, D. Vrinceanu, and V. N. Ostrovsky, J. Phys. B **38**, S279 (2005).

[12] Arne Schwettmann, Jeff Crawford, K. Richard Overstreet, and James P. Shaffer, Phys. Rev. A, **74**, 020701 (2006).

[13] Arne Schwettmann, K. Richard Overstreet, Jonathan Tallant, and James P. Shaffer, J. Mod. Opt., **54**, 2551 (2007).

[14] K. Richard Overstreet, Arne Schwettmann, Jonathan Tallant, and James P. Shaffer, Phys. Rev. A, **76**, 011403 (2007).

[15] P. Goy, J. M. Raimond, G. Vitrant, and S. Haroche, Phys. Rev. A. **26**, 2733 (1982).

[16] Thomas F. Gallagher, *Rydberg Atoms* (Cambridge University Press, 1994).

[17] C. Laughlin and G. A. Victor, Adv. At. Mol. Phys. **25**, 163 (1988).

[18] M. Marinescu, H. R. Sadeghpour and A. Dalgarno, Phys. Rev. A. **49**, 982 (1994).

[19] Xinghong He, Baiwen Li, Aiqiu Chen, and Chengxiu Zhang, J. Phys. B, **23**, 661 (1990).

[20] J. W. Farley and W. H. Wing, Phys. Rev. A, **23**, 2397 (1981).

[21] M. L. Zimmerman, M. G. Littman, M. M. Kash, and D. Kleppner, Phys. Rev. A **20**, 2251 (1979).

[22] Hans A. Bethe and Edwin E. Salpeter, *Quantum Mechanics of One- and Two-Electron Atoms* (Plenum, 1977).

[23] J. Dalibard and C. Cohen-Tannoudji, J. Opt. Soc. Am. B. **6**, 2023 (1989).

[24] H. J. Metcalf and P. van der Straten, *Laser Cooling and Trapping* (Springer, 1999).

[25] C. G. Townsend, N. H. Edwards, C. J. Cooper, K. P. Zetie, C. J. Foot, A. M. Steane, P. Szriftgiser, H. Perrin and J. Dalibard, Phys. Rev. A **52**, 1423 (1995).

[26] C. E. Wieman and L. Hollerg, Rev. Sci. Instrum. **62**, 1 (1991).

[27] M. A. Clifford, G. P. T. Lancaster, R. S. Conroy, and K. Dholakia, J. Mod. Opt. **47**, 1933 (2000).

[28] J. Tallant, K. R. Overstreet, A. Schwettmann, and J. P. Shaffer, Phys. Rev. A, **74**, 023410 (2006).

[29] D. A. Dahl, Simion 3D v7.0, Idaho National Engineering Laboratory, ID (1996).

[30] M. Marinescu, H. R. Sadeghpour, and A. Dalgarno, Phys. Rev. A **49**, 982 (1994).

[31] K. H. Weber and C. J. Sansonetti, Phys. Rev. A **35**, 4650 (1986)

[32] P. Goy, J. M. Raimond, G. Vitrant, and S. Haroche, Phys. Rev. A **26**, 2733 (1982)

[33] Sesko D. W., Walker T. G. and Wieman C. E., J. Opt. Soc. Am. B. **8**, 946 (1991).

[34] Drewsen M. Laurent P., Nadir A., Santarelli G., Clairon A., Castin Y., Grison D. and Salomon C., Appl. Phys. B **59**, 283 (1994).

[35] Grego S., Colla M., Fioretti A., Muller J. H., Verkerk P. and Arimondo E., Opics Comm. **132**, 519 (1996).

[36] Gabbanini C., Evangelista A., Gozzini S., Lucchesini A., Fioretti A., Muller J. H., Colla M. and Arimondo E., Europhys. Lett. **37**, 251 (1997).

[37] Vorozcovs A., Weel M., Beattie S., Cauchi S. and Kumarakrishnan A., J. Opt. Soc. Am. B **22**, 943 (2005).

[38] Smith L. M., Keefer D. R. and Sudharsanan S. I., J. Quant. Specrosc. Radiat. Transfer **39**, 367 (1988).

[39] Dribinski V., Osssadtchi A., Mandelshtam V. A. and Reisler H., Rev. Sci. Instrum. **73**, 2634 (2002).

[40] Hillenbrand G., Foot C. J. and Burnett K., Phys. Rev. A **50**, 1479 (1994).

[41] Bracewell R. N., *The Fourier Transform and Its Applications* (McGraw-Hill, 2000).

[42] Strickland R. N. and Chandler D. W., Appl. Optics **30**, 1811 (1991).

[43] Kawata S. and Ichioka Y., J. Opt. Soc. Am. **70**, 768 (1980).

[44] Golub G. H.,Hansen P. C. and O'Leary D. P., SIAM J. Matrix Anal. Appl. **21**, 185 (1999).

[45] M. N. R. Ashfold, C. M. Western, L. Schnieder, W. Meier, and K. H. Welge, J. Chem. Phys. **92** 7027 (1990).

[46] H. Xu, N. E. Shafer-Ray, F. Merkt, D. J. Hughes, M. Springer, R. P. Tuckett, and R. N. Zare, J. Chem. Phys. **103**, 5157 (1995).

[47] H. J. Worner, T. P. Softley, and F. Merkt, Phys. Rev. Lett. **92**, 033005 (2004).

[48] E. Nikitin, E. Dashevskaya, J. Alnis, M. Auzinsh, E. R. I. Abraham, B. R. Furneaux, M. Keil, C. McRaven, N. Shafer-Ray, and r. Waskowsky, Phys. Rev. A. **68**, 023403 (2003).

[49] J. Oberheide, P. Wilhelms, and M. Zimmer, Meas. Sci. Technol. **8**, 351 (1997).

[50] M. Mons and I. Dimicoli, J. Chem. Phys., **90**, 4037 (1988).

[51] M. P. Robinson, B. L. Tolra, M. W. Noel, T. G. Gallagher, and P. Pillet, Phys. Rev. Lett. **85**, 4466 (2000).